3-9-2009

Non-Destructive Evaluation of Aerospace Composites

Jeremy D. Johnson

NON-DESTRUCTIVE EVALUATION OF AEROSPACE COMPOSITES

THESIS

Jeremy D. Johnson, Captain, USAF

AFIT/GMS/ENP/09-M02

DEPARTMENT OF THE AIR FORCE
AIR UNIVERSITY

AIR FORCE INSTITUTE OF TECHNOLOGY

Wright-Patterson Air Force Base, Ohio

The views expressed in this thesis are those of the author and do not reflect the official policy or position of the United States Air Force, Department of Defense, or the United States Government.

AFIT/GMS/ENP/09-M02

NON-DESTRUCTIVE EVALUATION OF AEROSPACE COMPOSITES

THESIS

Presented to the Faculty

Department of Engineering Physics

Graduate School of Engineering and Management

Air Force Institute of Technology

Air University

Air Education and Training Command

In Partial Fulfillment of the Requirements for the

Degree of Master of Science in Materials Science

Jeremy D. Johnson, BS

Captain, USAF

March 2009

AFIT/GMS/ENP/09-M02

NON-DESTRUCTIVE EVALUATION OF AEROSPACE COMPOSITES

Jeremy D. Johnson, BS

Captain, USAF

Approved:

_____/signed/_____	_____
Matthew J. Bohn (Chairman)	Date
_____/signed/_____	_____
Nancy C. Giles (Member)	Date
_____/signed/_____	_____
James L. Blackshire (Member)	Date
_____/signed/_____	_____
Douglas T. Petkie (Member)	Date

Abstract

Five methods of non-destructive material evaluation (NDE) were used to inspect various forms of damage commonly found in aerospace fiberglass composites: voids, edge and sub-surface delaminations, surface burning, and cracking. The images produced by X-ray, X-ray Computed Tomography, terahertz (THz) imaging, ultrasound, and flash IR thermography were analyzed for the detection of defects. Test results and analysis of each NDE method's capabilities provide a comparison study of conventional techniques versus the emerging technology of THz imaging for the non-destructive evaluation of aerospace composite materials. A comparison guide to the five methods' damage detection effectiveness for fiberglass composites is provided by defect type.

Acknowledgements

I would like to express my sincere thanks and appreciation to my research advisor, Lt Col Matthew Bohn, for his guidance, motivation, and exceptional laboratory prowess. His patient dedication to my learning, understanding, and achievement made an enormous impact on the outcome of this research. I would also like to thank Dr. Jim Blackshire of AFRL/RXLP for his expert guidance and for providing the materials and equipment to complete the job. I am also indebted to the NDE lab technicians Dan Laufersweiler and Dave Roberts of AFRL/RXSA as well as Dan Daniels of AFRL/RXLP for guiding my test setups and procedures with expert advice.

Table of Contents

Page

Page

Page

List of Figures

Figure Page

List of Tables

Table Page

NON-DESTRUCTIVE EVALUATION OF AEROSPACE COMPOSITES

I. Introduction

Recent advances in imaging technologies involving terahertz radiation have introduced new possibilities for the field of non-destructive evaluation and inspection. Terahertz radiation technology, in both the continuous wave (CW) and pulsed wave forms, has been used in sensing and imaging systems that have been demonstrated to safely and effectively inspect packages, baggage, and personnel for dangerous or harmful materials and chemicals [1, 2]. Recent research efforts have taken this inspection technique and applied it to the imaging and evaluation of various dielectric materials to include human cancer cells [3], food products [4], and polymer matrix composites (PMCs) [5, 6, 7]. This thesis provides a comparison study of pulsed terahertz imaging versus conventional imaging methods for the non-destructive evaluation (NDE) of aerospace composites.

1.1 Background

Fiber-reinforced composites are defined as materials consisting of high strength and modulus fibers embedded in or bonded to a matrix (resin) with distinct boundaries between them forming layers [8]. The fiber reinforcement is either in long, continuous strands or is chopped short and provides the material with strength, stiffness, and durability while the matrix provides such physical properties as heat resistance, UV

protection, and corrosion resistance. Both fibers and matrix retain their physical and chemical properties, while combining to produce a material with properties that could otherwise not have been achieved with either constituent alone.

The role of composites in aerospace applications has changed dramatically in the past twenty years evolving from secondary to primary airframe structures as the materials and processing technologies have matured. The development of reinforcement materials such as fiberglass, carbon fiber and aramid fiber (Kevlar), which exhibit superior strength-to-weight ratios than steel while being non-conductive and chemically inert, has accelerated the use of composites in high performance aircraft. According to the National Materials Advisory Board's 1997 report on the aging of U.S. Air Force aircraft:

> First generation glass-reinforced composites, in the form of thin-face sheet honeycomb sandwich constructions, have been in general use for secondary structures (i.e., wing-to-body fairings, fixed-wing and empennage cover panels, and secondary control surfaces) on Air Force commercial transport aircraft since the 1960s….The Air Force has…recently made significant use of composite primary structure on the B-2 and … F-22. [9:76]

Today, composite materials make up over a third of the weight of modern aircraft such as the V-22 Osprey, F-35 Lightning II, and Boeing 787 Dreamliner shown in Figure 1 below.

(a) (b) (c)

Figure 1. (a) V-22 Osprey, (b) F-35 Lightning II, and (c) Boeing 787 Dreamliner.

Composites have made the transition from minor subsystem parts to primary engineering structures. Large scale applications became feasible once the technical community was able to accurately model the materials' performance and damage development processes. Decades of research has identified the critical defect and damage modes as well as how the interaction of these progress from initial to final states of the material [10]. Such knowledge mitigated the risks associated with replacing heavy metal structures with lightweight composite structures. However, the composite structures continue to require regular inspection and evaluation to detect and prevent critical defects. This is necessary because composite components are far more susceptible to catastrophic failure than their metal counterparts.

Although industrial production methods continue to improve, cured composites inherently contain multiple internal defects such as voids, delaminations, and non-uniform fiber orientation/concentrations. While the material is in service, some or all of these defects will negatively affect its performance. During production, it is common practice to use non-destructive testing and evaluation (NDT&E) to detect any critical material defects and evaluate production quality. It is recommended that these tests be repeated periodically throughout the part's service life to monitor material health. However, there is neither an industry standard for test method nor standard criteria for differentiation between critical and noncritical defects [8]. Selecting the method and evaluation criteria are of considerable concern to the aerospace industry.

There are four main issues to consider before selecting a NDT&E method:

1. Identification of the *types* of defects to be detected as no single method can identify and evaluate the criticality of every type of defect.

2. Identification of the *size* of defect to be detected as critical size varies for each different material composition and defect type.
3. Determination of the relevant testing *environment*. For example, ultrasound is not effective for high temperature environments; and x-ray CT is ineffective for inaccessible or excessively large parts.
4. Determination of NDT&E equipment and trained personnel *availability* as these can become very limited due to cost.

Conventional evaluation methods such as ultrasound, radiography, and thermography have evolved and grown more advanced in recent years while gaining considerable prominence in material characterization and production quality control. A relative newcomer, terahertz (THz, T-ray) imaging was first introduced in 1995 as a potential alternative NDE technique [11]. As THz technology matures, it continually gains new applications and offers new insights into micro-structure and may soon challenge the conventional NDE methods for inspecting non-conducting materials such as polymer matrix composites.

1.2 Problem Statement

Aerospace vehicles are made of high performance and novel materials. They are used in applications where material effectiveness is critical. The increased complexity of new materials requires a more thorough and detailed knowledge of micro-structure, thus increasing the importance of developing more flexible and powerful non-destructive methods of material evaluation and component inspection. Without industry standards for NDE techniques, it is necessary to evaluate all techniques to determine the most effective inspection and evaluation process.

1.3 Research Objective

The objective of this research effort is to compare the non-destructive evaluation capabilities of THz radiation with the conventional NDE techniques of X-ray, X-ray CT, ultrasound, and flash IR thermography. Each technique will be applied to the non-destructive evaluation of delaminated, burned, or damaged fiberglass composite samples. The features and capabilities of the five different NDE methods and their respective advantages and disadvantages will be explored and a comparison of the results provided.

1.4 Experimental Approach

In parallel efforts, all five fiberglass composite test samples depicted in Figure 2 were evaluated by the NDE techniques: X-ray radiography, X-ray Computed Tomography (X-ray CT), ultrasound, IR thermography, and pulsed THz imaging. Although I performed many scans of the samples with the THz imaging system, all of the THz images used in this thesis were produced by Dr. Stoik [7].

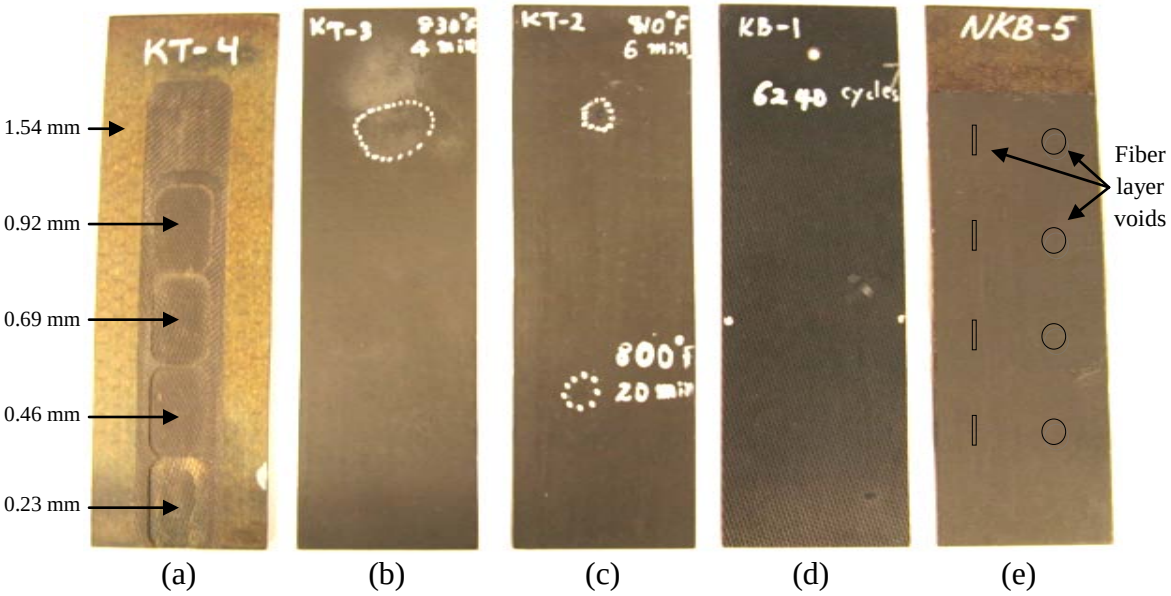

Figure 2. Fiberglass composite test samples measuring 2 in. x 6 in. with (a) thickness variation, (b) and (c) burn damage, (d) bend damage, and (e) sub-surface voids and side delamination.

1.5 Assumptions/Limitations

This research effort was limited by composite sample availability. Operationally representative fiberglass composite samples containing manufactured damage sets of common aerospace defects were used in this research. Operationally representative samples of carbon fiber and aramid fiber composites could not be fabricated within the time constraints of the research herein reported.

Prior knowledge of the samples' damage location was assumed since the THz system used was only capable of scanning a 2 cm. x 2 cm. square area. THz imaging was thus limited to areas containing known surface or sub-surface defects. Fast scanning commercially available THz systems were not available to be employed. Although the rate at which the THz imaging data was taken precludes this specific test setup from operational consideration, the results demonstrate the NDE capabilities of THz imaging.

1.6 Preview

In the following chapters, this thesis will present each NDE technique, the methods for data collection, and the results and analysis of composite material testing. Chapter 2 outlines the theory of signal generation, propagation, and detection for each NDE method while offering some brief background information. Chapter 3 describes the data collection procedures. In Chapter 4, the test results are presented and analyzed. Chapter 5 summarizes the results and provides a comparison of the presented NDE methods with recommendations for their use in testing aerospace composite materials.

II. Theory

This chapter provides a basic theoretical background to help the reader better understand the nature of the materials and technologies used. The first section explores some of the unique challenges in evaluating aerospace composites including a brief treatment of the wave scattering effects caused by propagating electromagnetic radiation through composite materials. Sections 2.2 through 2.6 introduce each of the five NDE methods used including how each is operationally applied to detect the various defects encountered in aerospace fiberglass composites. Each method will be broken down into the basic steps common among all of them: signal generation, signal propagation, and signal detection.

2.1 Aerospace Composite Materials

The aerospace industry uses multiple composite material types including both metal matrix composites (MMCs) and polymer matrix composites (PMCs). The most recent advances in PMC materials have been in reinforcing an epoxy or polyimide matrix with graphite (carbon) or aramid (Kevlar) fibers at fiber volume fractions ranging between 45 – 60%. These advanced composites provide much greater strength and durability than fiberglass, but at a substantially higher cost.

Regardless of which fiber used, reinforced plastics must be treated significantly different from metals when it comes to NDE as they generally have low thermal and electrical conductivities and high acoustic attenuation [12]. With such widely varying properties among composite materials, choosing an NDE method to detect inclusions, delaminations, poor fiber alignment, density, and porosity in anisotropic material has

been a daunting task—one that invariably leads to the use of multiple inspection methods to establish high levels of confidence in material quality.

For example, the predominant test method for crack detection, eddy current inspection, is also capable of detecting fiber orientation and volume fraction defects but cannot provide density or porosity information. Additionally, this method of using time-varying magnetic fields to induce electrical conduction paths is limited to those materials with adequate electrical conductivities. Only carbon and boron-based PMCs are capable of being examined by eddy currents. Fiberglass and aramid composites must then be inspected via optical, acoustic, thermal, or vibrational methods. Each of these methods have their own set of challenges.

One of those challenges is that the heterogeneous nature of composites causes a serious problem for predicting optical and acoustic transmittance through the material because the fibers have widely varying dielectric properties from the resin matrix. Effective Medium Approximation (EMA) theory provides the means by which a composite's *effective* dielectric properties can be calculated (Figure 3).

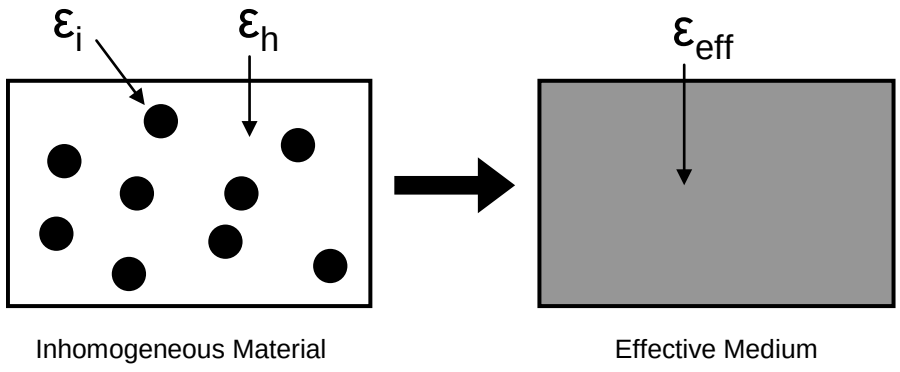

Figure 3. Effective mediums approximate the bulk properties of inhomogeneous systems.

The three most common EMA theories are the simple effective medium approximation, the Maxwell-Garnett theory, and the Bruggeman theory [13, 14]. These three EMAs are outlined and employed for these fiberglass samples in Stoik's dissertation on the Nondestructive Evaluation of Aerospace Composites Using Terahertz Time Domain Spectroscopy [7].

2.2 Electromagnetic Radiation Scattering Effects

Scattering is the physical process that describes the forced deviation of electromagnetic radiation from its straight trajectory due to non-uniformities in the medium through which it travels. Mie-Debye scattering and Rayleigh scattering are the two types of elastic radiation scattering. Rayleigh scattering describes the scatter of light by objects much smaller than a tenth the wavelength of incident light. This theory is more accurate in describing the scatter of light through gases or liquids and explains why the sky appears blue. The Mie-Debye solution to scattering utilizes Maxwell's equations and infinite sums to approximate the deviation due to any size of obstruction assuming an isotropic, homogeneous material and that the obstructions are spherical or infinite cylinders [15]. The Mie-Debye scattering theory will be briefly introduced since a few of the defects (scattering sources) we wish to detect are comparable to the THz radiation wavelengths which, for the system demonstrated, range from 0.2 mm to 1.5 mm.

To use the Mie-Debye solution, we must treat our composite material as a homogeneous effective medium as described previously at the end of section 2.1. Defects such as voids, inclusions, and cracks must be approximated to be of homogeneous spherical or cylindrical shape. With these assumptions made, we can approximate the transmission of scattered radiation.

For perpendicular incidence upon a cylindrical obstruction, the scattered wave will be polarized the same way as the incident radiation and propagate in that plane perpendicular to the cylinder's surface that includes the incident ray [16]. Perpendicularly scattered radiation is likely to be lost, not captured by a detector. Milton Kerker explains it this way:

> This effect can be observed when a cylinder such as a spider fiber is illuminated by a narrow parallel beam at perpendicular incidence. The fiber will appear to be brilliantly illuminated as long as the observer is in the appropriate plane. Otherwise, it will be lost to sight. [16:263]

The reflected intensity of radiation perpendicularly incident upon a cylindrical obstruction is approximated by:

$$I = I_o \frac{\pi^4 a^4}{\lambda^3 r}(m^2 - 1)^2 \tag{1}$$

where *a* is the obstruction radius, *r* is the distance from the center of obstruction, and *m* is the ratio of the refractive indices—obstruction to containing medium.

For linearly polarized light (as from a THz emitter) incident upon an infinitely long cylindrical obstruction, the intensities of vertical and horizontal components of the reflected beam are given by:

$$I_v = I_o \frac{2\pi^4 a^4}{\lambda^3 r}\left(m^2 - 1\right)^2 \sin^2(\chi) \tag{2}$$

$$I_h = I_o \frac{4\pi^4 a^4}{\lambda^3 r}\left(\frac{m^2 - 1}{m^2 + 1}\right)^2 \cos^2(\chi)\cos^2(\theta) \tag{3}$$

Where χ is the angle of the reflected beam's now cylindrical polarization with respect to the positive horizontal axis and θ is the radial reflection angle away from initial propagation direction as depicted in Figure 4 [7].

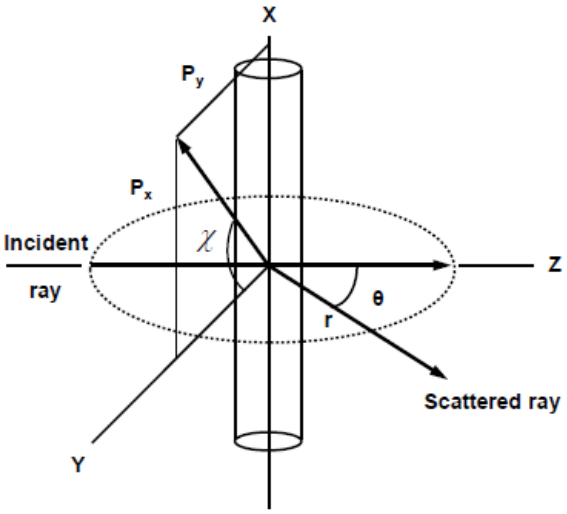

Figure 4. Scattering of radiation off an infinite cylinder [16].

Small spherical obstructions (small relative to radiation wavelength) scatter radiation according to the proportionality:

$$I = I_o \frac{16\pi^4 a^6}{\lambda^4 r^2}\left(\frac{m^2-1}{m^2+2}\right)^2 \tag{4}$$

The inverse square of distance *r* greatly hinders our detection efforts, but we are aided by the raising of obstruction radius *a* to the sixth power [16:34].

2.3 Radiography

Radioscopic inspection remains the most powerful and widely used NDE method for inspecting industrial and commercial materials [17]. It provides a two dimensional, superimposed projection of a three dimensional body and is able to be displayed on film, camera, or computer screen. The image produced is a contrast map of material thickness and density. The term radiography includes both broadband X-ray and discrete frequency gamma-ray inspection modes as well as the high energy beta and neutron techniques for dense materials. The wavelengths associated with radiography are on the

order of nanometers offering high resolution imaging of material density variations. Fiber-reinforced polymer matrix composites generally have low molecular weights so they don't absorb high energy X-rays. Medium energy X-rays were thus used in this research for good penetrating power while maintaining some material absorption and diffraction effects for sufficient image contrast.

X-ray computed tomography (CT) involves rotating the object 360° within the radiation beam to combine the many X-ray absorption profiles into a three dimensional, cross-sectional X-ray absorption map by incremental slices. Although time-consuming and object size limited, CT allows cross-sectional slice-by-slice evaluation of the object's internal structure.

2.3.1 X-Ray Generation

X-rays are the product of the acceleration (using synchrotrons) or deceleration (Bremmsstrahlung) of electrons. The most cost efficient manner to generate X-rays is to use a modular, portable *X-ray tube* that directs an electron beam onto a large target anode. Common anode materials are the high atomic weight metals: molybdenum, tungsten, and rhenium. Radiation is emitted from the target perpendicular to the incident electron beam at energies proportional to the electron gun bias voltage and the material absorption path. The result is a relative point source of X-rays at varied energies as depicted in Figure 5.

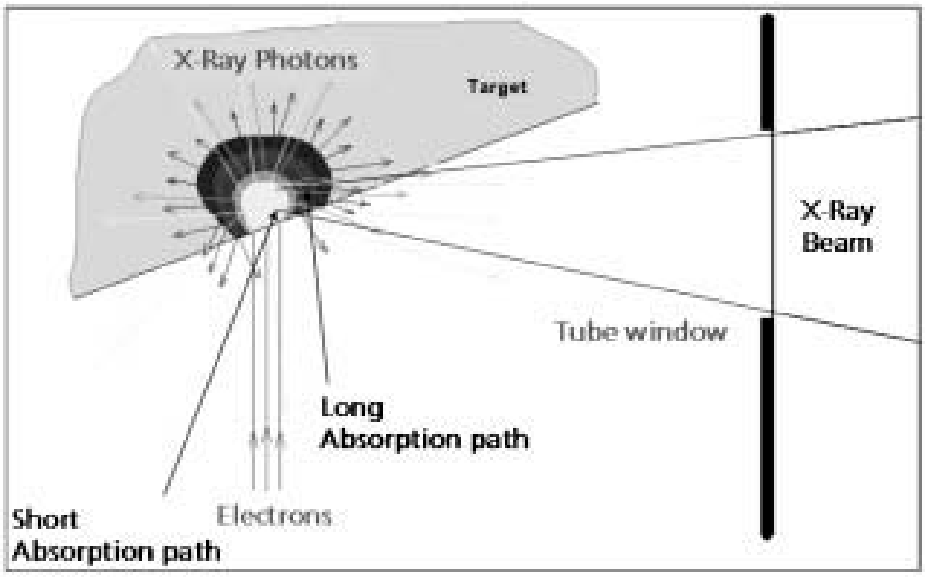

Figure 5. X-ray generation by electron deceleration through a high atomic weight metal anode [17].

2.3.2 X-Ray Propagation

The varied absorption and scatter of X-rays along the plane of incidence provides the basis for locating defects such as cracks, porosity variations, and cross-sectional density variations (voids and non-uniform fiber distribution) within the object [8]. The absorption depends upon three factors: material thickness, density, and incident radiation intensity. The measured intensity at the detector is governed by Beer's law of radiation attenuation:

$$I = I_o e^{-\mu X} \tag{5}$$

where I is the measured radiation intensity, I_0 is the incident intensity, μ is the attenuation coefficient which includes losses due to scattering and absorption, and X is the medium's optical cross-section thickness.

2.3.3 X-Ray Detection

Digital X-ray detectors have quickly replaced photographic film in all but a few industries. Today's detectors utilize a scintillator in front of an array plate of silicon-based semiconductor optical sensors. The scintillator layer converts the X-ray photon intensity distribution into local signals of visible light which are then converted into a contrasting shadowgraph by the silicon detector. The shadowgraph image, a two dimensional projection of the object, is then captured by a camera or sent to a computer for display.

These superimposed projections reveal the object's internal structure as well as other artifacts that may or may not be real. Some of the lighter contrasting artifacts are due to the high dynamic range of X-ray intensities caused by the generation technique in conjunction with propagation attenuation, absorption, and scatter. Further evaluation is often necessary to validate the presence of small defects due to such high resolution. Specifically, X-ray absorbing dyes and penetrants are used when thin cracks are suspected in order to increase contrast and expand the damage area for visual acuity.

2.4 Ultrasound

Ultrasonic inspection is the most widely used method of NDE for composite materials [18]. Ultrasound frequencies are just above the audible range of humans beginning at 20 KHz and ending near 50 MHz. The use of ultrasound as an NDE method first began in the early 1970's. It exploits the ability of high energy sound waves to detect the presence of defects and interfaces within a medium by the attenuation of the ultrasonic waves. While ultrasonic imaging is used worldwide in medical applications, material evaluation requires a much finer resolution. For material evaluation, the higher

frequency range of 0.5 MHz – 25 MHz is used. Higher frequencies provide better resolution and defect detection capability but are attenuated by material absorption more than lower frequencies resulting in a trade-off of penetrating power versus resolution.

There are three main scanning mechanisms and many ultrasonic inspection systems are capable of performing all three simultaneously. As seen in Figure 6, the A-Scan is a waveform display that plots voltage signal amplitude along a timeline, the time of flight (TOF) of the acoustic wave. The first pulse echo is a reflection from the sample's front surface. The third pulse in Figure 6 corresponds to the back surface, while any interior defects would appear as echoes between these two pulses at heights proportional to the size, depth, and geometry of the defect.

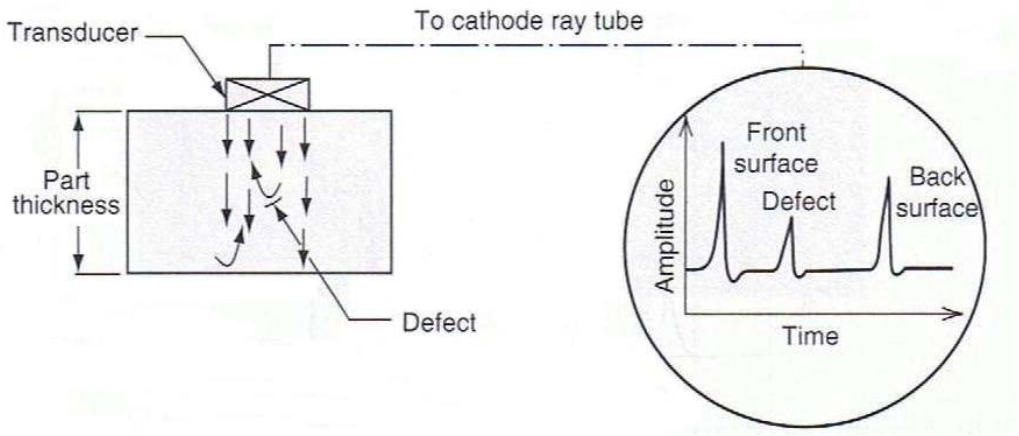

Figure 6. Pulse-Echo Method of ultrasonic inspection with A-Scan output [8].

The B-Scan is roughly your *side view* in that it profiles the sample showing light spots (no signal data) in areas beneath a defect, signal amplitude being proportional to depth. The C-Scan, a popular manufacturing inspection tool, provides a *plan view* of A-scans (either local amplitude or TOF values) with defects appearing as low signal/high attenuation areas—dark patches in grey-scale.

The next two sections provide brief descriptions of ultrasonic wave generation, propagation and detection for a pulse-echo method ultrasound technique, depicted previously in Figure 6. Benefits to using the pulse-echo method include its ability to provide depth information as well as its utility as an in-place inspection tool not requiring the removal of the part from its assembly.

2.4.1 Ultrasonic Wave Generation

The ultrasonic waves are generated by electrically exciting a piezoelectric transducer which converts a pulsed voltage signal into mechanical vibrations producing acoustic energy pulses. Generally, a narrow spike pulse is used to generate a short burst of ultrasound.

2.4.2 Ultrasonic Wave Propagation

The acoustic waves propagate into the test item's surface through a coupling medium, usually water. The coupling medium allows a much greater amount of energy to be transmitted through the material and less reflected from its front surface. While total immersion of the test item ensures uniform coupling, it is not always feasible to do so. In such cases, water or gel is generously applied to the region under evaluation.

The ultrasonic waves are scattered, absorbed, and dispersed by the coupling medium as well as by the test material's elasticity thereby limiting the depth of penetration for a given material. However, material interfaces and defects reflect and further attenuate the waves allowing only near-surface detection within thick elastic material test items.

At interfaces, the sound energy reflected or transmitted depends upon each medium’s acoustic impedance [18]. For an interface between water and fiberglass

composite, expect half the energy to be reflected; whereas for a composite/air interface, such as a void or delamination, expect nearly 0% transmission since the double interface acts as an acoustic resonator trapping much of the signal inside. It is this high degree of signal attenuation that allows ultrasound to pick out void and delamination defects. Other defects such as inclusions, porosity, and cracking must exhibit sufficient acoustic impedance or signal scattering to be detected.

2.4.3 Ultrasonic Wave Detection

In the pulse-echo technique, the reflected waves are detected by the same piezoelectric transducer that generated the wave, converting the incoming vibrations into an electronic signal. Both the signal amplitude and TOF of the waveform is then able to be analyzed for each of the different modes (A-scan, B-scan, C-scan, etc). For our purposes, C-scan amplitude plan images will be the primary data source as the slight warping of our samples greatly affects ultrasonic TOF data.

In general, artifacts larger than a tenth of the acoustic wavelength will contribute to signal scattering and should be detectable [18]. However, depending upon feature orientation with respect to the sound wave and the system's signal to noise ratios, defects as large as five times wider than the wavelength might not be detected [19]. Although the pulse-echo method is limited to the detection of only the first occurring defect, only one of the test samples contains overlapping defects (sub-surface void sample). Another source of confusion in ultrasonic inspection is that sub-surface voids are indistinguishable from resin rich zones. An example of this will be presented in Chapter 4.

2.5 Thermographic Inspection

Infrared (IR) thermography is an active inspection method based on the thermodynamics of materials in that it characterizes the diffusion of heat from an object's surface. Defects and non-uniform fiber distributions within composite materials cause local variations in the material's thermal conductivity providing detection capability.

2.5.1 Thermal Front Generation

The heating of the sample is accomplished via conductive (hot plate), convective (oven), or radiative (flash lamp or laser) means. For thick objects or materials which require a prolonged and uniform heat source, the common thermographic method is to apply a hot plate to one side of the test object and record the back surface transient temperature contours (thermograms). For thin composite structures (non-carbon), flash IR thermography is the NDE method of choice. In flash IR thermography, a high intensity photographic flash gun is used as the heat source. Flash IR thermography is a very fast and efficient NDE method performing sample scans in as little as ten seconds. However, it is limited to thin objects and materials that do not significantly reflect or laterally conduct the flash heat wave. Either property would prevent the heat wave from penetrating the surface. The flash must also be performed normal to the material's surface to produce a uniform thermal front. Flash IR thermography will be the only thermographic inspection method used in this research.

2.5.2 Thermal Front Propagation

When the flash heat front encounters the material's surface, a substantial amount of thermal energy is reflected or absorbed by the surface. From the surface, the thermal

wave propagates through the material according to the material's thermal properties. The surface temperature then decreases uniformly unless a discontinuity resists the heat flow.

Defects within the material can either increase or decrease the rate of heat flow. The presence of air pockets or porosity, for example, decreases both the density and thermal conductivity of the material resisting the thermal front propagation. For an air bubble volume fraction φ, the *effective* conductivity k of a porous material is given by:

$$k = k_m \left(\frac{k_a(1+2\varphi) + 2k_m(1-\varphi)}{k_a(1-\varphi) + k_m(2+\varphi)} \right) \tag{6}$$

where conductivities k_m and k_a are that of the homogeneous matrix material and air, respectively. The thermal diffusivity α of the effective material is then the effective conductivity divided by the heat capacity (ρc),

$$\alpha = \frac{k}{\rho c} \tag{7}$$

with density ρ and specific heat c [20]. The material's thermal emissivity β, a measurement of the ability to absorb or emit thermal radiation, is given by:

$$\beta = \sqrt{k \rho c} \tag{8}$$

Defects in the material alter the conductivity, density, and/or heat capacity thus changing the emissivity. These changes affect the material's surface temperature which is approximated below as a 1D function of the initial temperature T_0 [K], the emissivity β [m], and the energy absorbed by the surface Q [J/m^2] assuming no lateral energy losses:

$$T(t) = T_0 + \frac{Q}{\beta \sqrt{\pi t}} \tag{9}$$

Any measured surface temperature variations can be compared to the expected time-dependent surface temperature of the material.

2.5.3 Defect Detection

The surface temperatures are recorded over time with either temperature sensitive paints or photographically using an IR camera. Commonly, the IR camera is co-located with the flash heat source. Defects such as delaminations and inclusions (foreign matter) are detected as increased local front surface temperatures while air voids and porosity are detected as decreased temperatures. Generally, the time derivatives of the recorded surface temperatures are used to construct images for material analysis.

2.6 THz Imaging

THz imaging is a relatively new investigative technique that is non-destructive, non-ionizing, non-contact, and non-invasive. The terahertz frequency range is from $1x10^{11}$ Hz to $1x10^{13}$ Hz and corresponds to millimeter wavelengths of light, from 3 mm down to 30 μm as depicted in Figure 7.

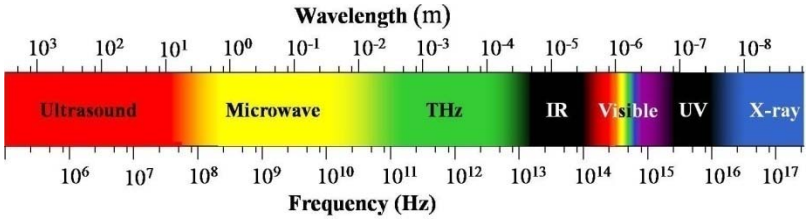

Figure 7. The THz region is bounded by microwave and long-wave IR frequency regions.

Waves of THz radiation (T-rays) are at very weak photon energies. The necessary field intensities for imaging are incredibly low posing few safety risks, while still providing surface, sub-surface, and three-dimensional (3D) structure information with sub-millimeter resolution [21]. Like microwave radiation, terahertz radiation is

capable of penetrating non-conducting materials like clothing, cardboard, wood, plastics, and ceramics, but it is quickly absorbed by polar substances like water which prevents its use in communications within earth's atmosphere. However, the use of THz technology has grown considerably over the past decade in scientific, medical, and security applications as it is non-harmful and capable of resolutions 50 times greater than microwave imaging.

THz frequencies are matched to molecular rotational resonant energies producing material responses not present at X-ray and acoustic frequencies. This unique phenomenon creates a THz-specific material signature fingerprint that allows for the detection of potentially harmful or dangerous materials [22]. T-rays, while unable to penetrate metals, can penetrate up to 5 mm of skin; but unlike X-rays, THz radiation is incapable of ionizing an atom so it poses no more risk to human cells than radio waves. These qualities have led to the application of THz-based systems in airport security as well as non-invasive epithelial and breast cancer detection [3, 23]. Figure 8 shows a pair of examples of current THz imaging systems' capabilities.

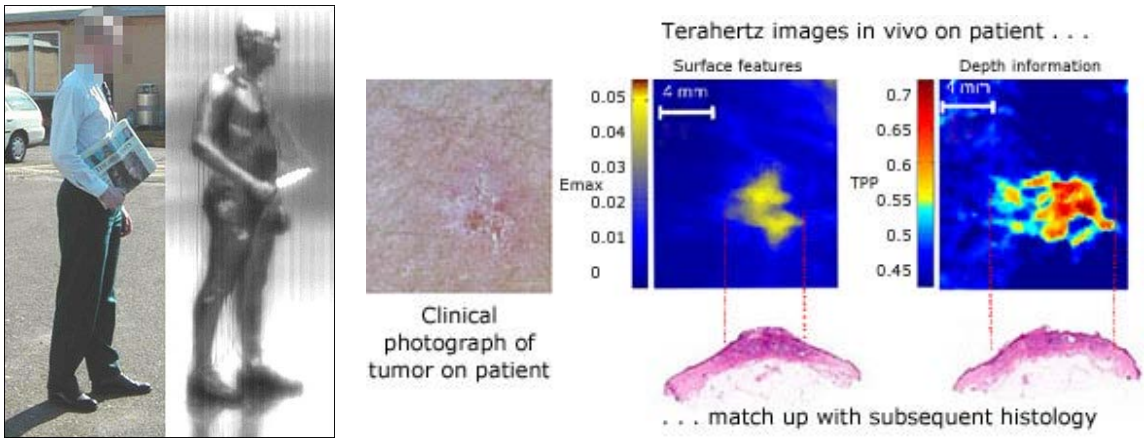

(a) (b)

Figure 8. T-ray imaging in (a) security and (b) biomedical applications [24, 25].

THz imaging systems employ either pulsed or continuous wave (CW) THz radiation. CW imaging has been around since the early 1970s while pulsed THz imaging was first introduced in 1995 by Hu & Nuss [11]. The CW THz imaging systems are much faster in forming images as they don't require time delay scanning. Additionally, they are much more compact and affordable while current pulsed THz imaging systems require complex optics and are very sensitive. However, pulsed systems provide much more evaluation capability. In a comparison study between pulsed and CW THz imaging systems, Nicholas Karpowicz explains their differences this way:

> Unlike pulsed THz imaging, CW imaging…only yields intensity data and does not provide any depth, frequency-domain or time-domain information about the subjects when a fixed-frequency source and a single detector are used. [26]

By measuring the TOF of reflected pulses, pulsed THz imaging is capable of structural evaluation with depth resolutions on the order of 100 μm, as the TOF of the reflected pulse directly correlates to dielectric interface locations along the beam's propagation line [27]. The phase information of the reflected pulse allows different materials to be easily discriminated based on their absorption coefficients and refractive indices. These non-destructive evaluation capabilities are enhanced when using a THz tomographic imaging system (T-ray CT) [28] that extracts not only its 3D structure but its frequency-dependent optical properties at much greater signal-to-noise ratios.

Both emission and detection are coherent, which means that both the amplitude and phase of the THz waveform are captured simultaneously. This allows a pulsed THz system to utilize time domain spectroscopy (THz-TDS) to determine the full, complex dielectric constant of the material while avoiding the uncertainties related to using the

Kramers-Kronig relations (unlike the TOF imaging predecessor Fourier Transform Spectroscopy) [11]. THz-TDS will be briefly presented later in this section.

2.6.1 Pulse Generation

The traditional technique for generating THz pulses is to focus an ultrashort (femtosecond) pulsed pump laser onto a photoconductive switch. One could use an electro-optic crystal as the THz emitter, but photoconductive (PC) switches have been found to be more efficient emitters when pumped at visible/near-IR frequencies [29]. A PC switch, depicted in Figure 9, is composed of two thin metal strip lines separated by roughly 50 µm and adhered to a semiconductor substrate, typically low-temperature grown GaAs (LT-GaAs) [30]. A bias voltage is applied across the strips creating a dipole switch with a strong depletion field near the anode. When an optical pulse at a sufficient wavelength to excite the semiconductor electrons is focused onto the gap, electrons from the semiconductor's valence band are excited into the conduction band allowing carriers to accelerate toward the anode resulting in a pulsed photocurrent along the switch.

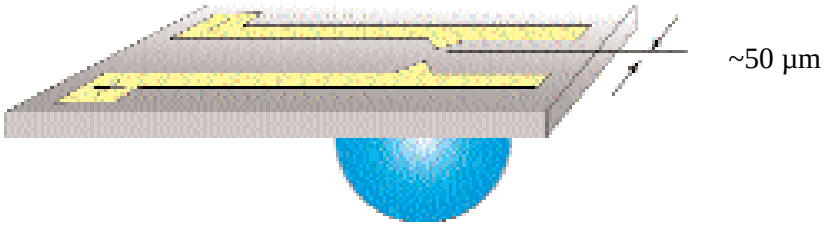

Figure 9. Photoconductive switch THz emitter with collimating spherical lens [31].

The time-varying pulsed current emits electromagnetic pulses in THz frequencies at the same repetition frequency as that of the femtosecond pump laser. The hemispherical silicon lens on the back side of the PC switch collimates the THz pulse

beam to later be focused onto the test sample. An on-off switching power supply (with a rate of ~100 kHz) is used to provide a bias voltage to the emitter. This technique has an added benefit over using a beam chopper in that it improves the signal-to-noise ratio (SNR) of the THz output by avoiding the noisy low frequency band.

2.6.2 Pulse Propagation

The THz pulses from the emitter are focused onto the test object via metal off-axis parabolic mirrors. The effective THz beam spot size has a wavelength dependent diameter given by

$$d \approx \frac{2 f \lambda}{d_o} \tag{10}$$

where f is the focal length of the mirror, λ the radiation wavelength, and d_o the collimated beam diameter incident on the mirror [7]. The radiation interacts with the surface via direct reflection, transmission, absorption, and scattering. The pulse radiation that is reflected provides surface characterization while the transmitted radiation is then able to provide the same interactions at deeper levels. Radiation transmitted through the surface will be partially reflected off any interfaces within the material to include the back surface-to-air interface. The reflected radiation from within the object, having a longer optical path length, arrives at the detector at a later time than that which was reflected off the front surface. The internally reflected radiation returns as a replica of the original pulse having a distorted phase, polarity, and amplitude. The return signal amplitudes provide absorption/transmission curves at all penetration depths and varies in both frequency and time.

When the propagating radiation encounters another medium of significantly differing dielectric properties, an interesting and useful optical phenomenon called Fabry-Perot resonance can occur (as in a mirrored Fabry-Perot etalon). A lower refractive index medium found within a medium of higher refractive index, such as an air pocket within a polymer, will act as a resonator *trapping* radiation within the layer. Partial energy waves at cavity-specific resonant frequencies escape the resonator with each reflection. Taking advantage of this phenomenon allows one to determine the dimensions of layers or voids within an object.

A major THz propagation challenge is the absorption and scatter of THz radiation. All materials absorb THz radiation to some degree which reduces the already weak signal power. Water (and therefore water vapor) is a strong THz absorber, so one must minimize the propagation distance from emitter to detector if working in a free air environment. Water absorption tables for THz frequencies are readily available [32]. In fact, absorption properties of most common chemicals and materials are fairly well known and their effects can be accounted for in system design or test procedure. However, radiation scatter effects are much more difficult to predict. See section 2.2 for a brief introduction to electromagnetic radiation scattering.

2.6.3 Pulse Detection

The THz pulse train can be detected with a second PC switch or by using an electro-optic (EO) sampling technique as was used in this research. This technique requires the reflected THz beam and probe beam be recombined and focused onto an EO detector crystal properly oriented for the probe beam's polarization. The THz waves modify the refractive index of the EO crystal, a phenomenon called the Pockel's Effect,

which creates a phase delay in the linearly polarized probe beam. This allows the pulse field strength E_{THz} to be measured as it is directly proportional to the phase delay $\Delta\Gamma$ given by:

$$\Delta\Gamma = \left(\frac{2\pi}{\lambda} d n_{opt}^3 r_{41} \right) E_{THz} \tag{11}$$

where d is the thickness of the EO crystal, n_{opt} is the group refractive index of the EO crystal at the wavelength λ of the probe beam, and r_{41} is the EO coefficient [33]. This phase delay also leads to a birefringence in the crystal which rotates the probe beam's polarization. By measuring the polarization shift, we can indirectly obtain both the phase delay and THz field strength. Figure 10 depicts the EO crystal detection scheme used for this research.

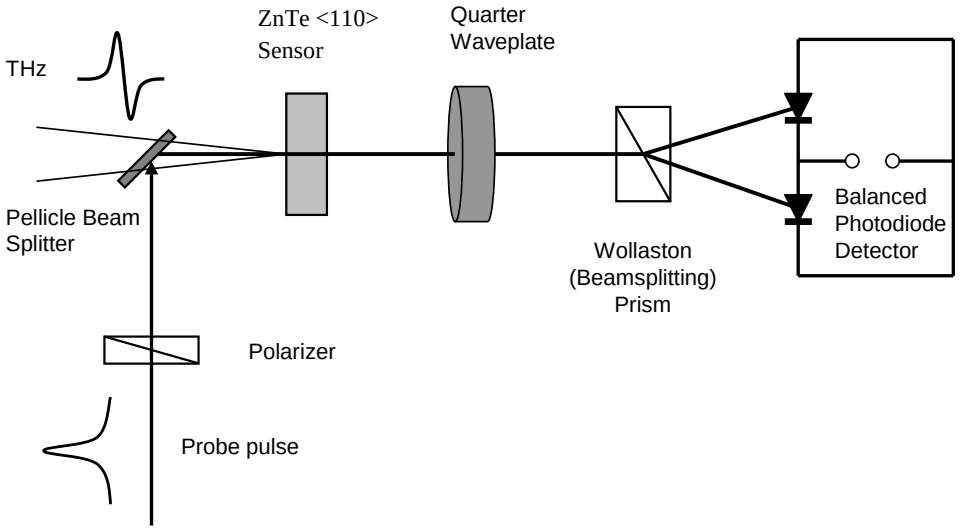

Figure 10. Setup for EO crystal detection of THz pulses [7].

The Pellicle beam splitter combines the probe beam with the THz beam and aligns their polarizations to be oriented with the <110> direction of the zinc telluride (ZnTe) crystal, while the quarter-wave plate is used to apply a $\lambda/4$ bias to the probe beam.

Then a Wollaston polarizer is used to convert the probe beam's phase delay into an intensity modulation between two linearly polarized, orthogonal beams. The subsequent photodiodes feed the signals to a lock-in amplifier referenced to the THz emitter frequency of 100 kHz.

2.6.4 THz Time Domain Spectroscopy

A major concern in pulsed THz imaging is the timing of the pulse through the detector. "The terahertz pulse is distorted by selective absorption as it passes through the sample, causing delays in its arrival time at the detector [31: 27]." The use of a mechanical delay line enables the probe beam pulse sections to arrive at the detector simultaneously with its corresponding interrogating pulse section, thus building an image of the pulse in the time domain.

The optical delay is achieved by using a retro-reflective mirror mounted on a Newmark NLS4 mechanical stage under computer control. The delay line used has a maximum speed of 2 in/s, resolution of 0.125 μm, and a repeatability of 5 μm [7]. The optical delay allows the time of flight (TOF) of the THz photons through the sample to be successively recorded. Fast Fourier transform (FFT) analysis then converts the time domain data into the frequency of THz arriving at the detector. This provides spectroscopic information about the scanned material.

III. Methodology

This chapter provides a description of the test equipment, test setup, and procedures used to evaluate the fiberglass composite samples with each NDE method. The evaluations were accomplished on USAF equipment under the close supervision of experienced physicists and NDI technicians to ensure that the methods and procedures were operationally representative of the aerospace industry.

3.1 Radiography Test Methods

3.1.1 Radiographic Setup

An X-TEK HMX 160 X-ray CT chamber, combined with X-TEK computer software, was used for all radiographic testing. The X-TEK system includes an automatic locking mechanism that will not allow the chamber to be opened while operating at high voltages and X-rays are present. Enclosed within the shielded chamber are an X-ray tube, a variable-element target, a three degree of freedom sample mount, and a digital detector. The detector is a semiconductor plate coated with scintillator material to effectively count the number of incident photons per pixel. The X-TEK produces electron beams with potentials of up to 160 kV. An 85 kV, 60 μA electron beam incident on a molybdenum target was used to generate the X-rays used in all of our radiographic testing.

3.1.2 X-ray Procedure

Each composite test sample was mounted vertically in a small metal vice arranged on the three DOF track. Using the computer software, the mount was rotated to orient the sample's face perpendicular to the incident X-rays. The sample was then moved to the end of the track closest to the detector to accommodate the size of the sample. This

allowed the entire sample to reside within the cone of X-rays to image the entire sample. The image to be created was set to be a 32 frame average at 1 fps. The chamber was then closed and high voltage applied. Within 45 seconds, a grey-scale radiographic shadow image of the sample appeared on the computer screen.

The white balance and contrast ratio were both altered to better view the artifacts. The image was saved once the number of artifacts visible was maximized. No effort was given to scan individual defect areas for greater image resolution.

3.1.3 X-ray CT Procedure

To take computed tomograhic images, the procedure varies only slightly from that of the X-ray scans. The two differences are both found within the software setup. Before the sample was placed within the chamber, reference shading data was taken twice over 64 frames at 2 fps to provide both a *white* and a *black* image, the *black* image formed by performing an empty chamber scan and the *white* image in the absence of X-rays. The other difference was in selecting 720 projections at 1 fps using 0.5° angle increments to provide a three-dimensional scan.

The 3D grey-scale image was then rotated as necessary to capture front, back, and side profile views. Each image plane was then inspected for defects by exterior and cross-sectional slice views, zooming through the image slice-by-slice (in 0.14 mm increments) adjusting the contrast as required before saving and exporting 2D images.

3.2 Ultrasound Test Methods

3.2.1 Ultrasound Setup

The immersive ultrasound system used was an AMDATA 5-Axis System with a thick, flat aluminum plate leveled about ten inches below the water's surface. A 5 MHz

transducer with a 3” focal length was used to generate and detect the acoustic pulses. The electrical signal sent to the piezoelectric transducer was a 250 V spike resulting in a short time duration, high amplitude acoustic pulse centered at a frequency of 5 MHz. The scan settings used included a software time-gate in order to only measure the reflected signal return from the aluminum plate. This ensured all measured signals had passed through the sample twice. Such a setup negated the signal return time variations experienced for warped samples. The image output settings were set to display C-scans of maximum positive amplitude signal values versus location. The normal resolution setting and one inch per second scan speed allowed a 2 in. x 6 in. sample to be scanned in just under five minutes.

3.2.2 Ultrasound Procedure

Each sample was secured above the aluminum plate by placing ½ in. thick lead weights above and below the ends. These weights appear in the C-scan images as triangular shapes at the ends of each sample. The 5 MHz transducer was immersed to a height of 3 inches above the sample. The transducer was then manually moved in the XY plane to find the X- and Y-axis scan limits. These positions were then input into the computer software and the scan begun.

3.3 Thermography Test Methods

3.3.1 Thermographic Setup

The flash IR thermography testing was accomplished at room temperature using Themal Wave Imaging, Inc’s ThermoScope II™ in conjunction with MOSAIQ 4.0 software. The ThermoScope II™ contains a flash lamp as its heat source and a high speed IR camera capable of recording images at a rate of 300 Hz. It produces a heat flash of 2-

30 ms duration; however, the thermal properties of the flash have not been disclosed nor were they measured for this research effort. Although the MOSAIQ 4.0 software is capable of displaying images of the raw surface temperature versus time, NDE is performed using the first and second time derivative thermal images.

For our thin composite samples, we set the flash duration to 4.9 ms and the capture rate to 60 Hz. The time-lapse photography of front surface temperature data was converted into thermal conduction videos; each test lasting approximately 10 seconds.

3.3.2 Thermography Procedure

The samples were set flat on two wooden slats to thermally isolate them. Care was taken to ensure the samples were positioned very near the camera's focal length for clear images. Every composite sample was tested beside the milled sample labeled KT-4 to correlate the thermal images with those at known thickness variations. Once recording was completed, the software converted the thermal images into first and second time-derivative thermal conduction videos which were played side-by-side in real-time. The videos were repeatedly re-wound and re-played slowly for close inspection. Select screen shots of each video are included in the results and analysis chapter of this thesis.

3.4 THz Test Methods

3.4.1 THz Imaging Setup

Approximately 30 mW of a 500 mW Coherent Mira 900-F Ti:sapphire laser mode-locked at a center wavelength of 800 nm with pulse durations of 97 - 110 femtoseconds (fs) and a repetition rate of 76 MHz was focused onto an EKSPLA LT-GaAs photoconductive switch emitter to produce ultrashort THz pulses with approximately 1 μW average power. The pulsed THz radiation was focused onto the

composite test sample which was then rastered across the stationary THz beam spot. Reflected THz radiation was collected and analyzed with respect to the original pulsed beam thus providing both spatial and time information which was used to produce tomographic images of the material's structure.

3.4.1.1 THz Beam Optics

As depicted in Figure 11, the THz emissions were collimated and focused onto the test sample by gold coated off-axis parabolic mirrors. The reflected THz beam was then collimated and refocused by another pair of mirrors onto the electro-optic zinc telluride (ZnTe) crystal. At the detector, the THz signal recombined with the reference probe pulse and was directed into New Focus balanced photodiodes (Nirvana Detector, Model 2007) that converted the optical signals into electrical waveforms for the lock-in amplifier. For additional information, see section 2.5 and [7].

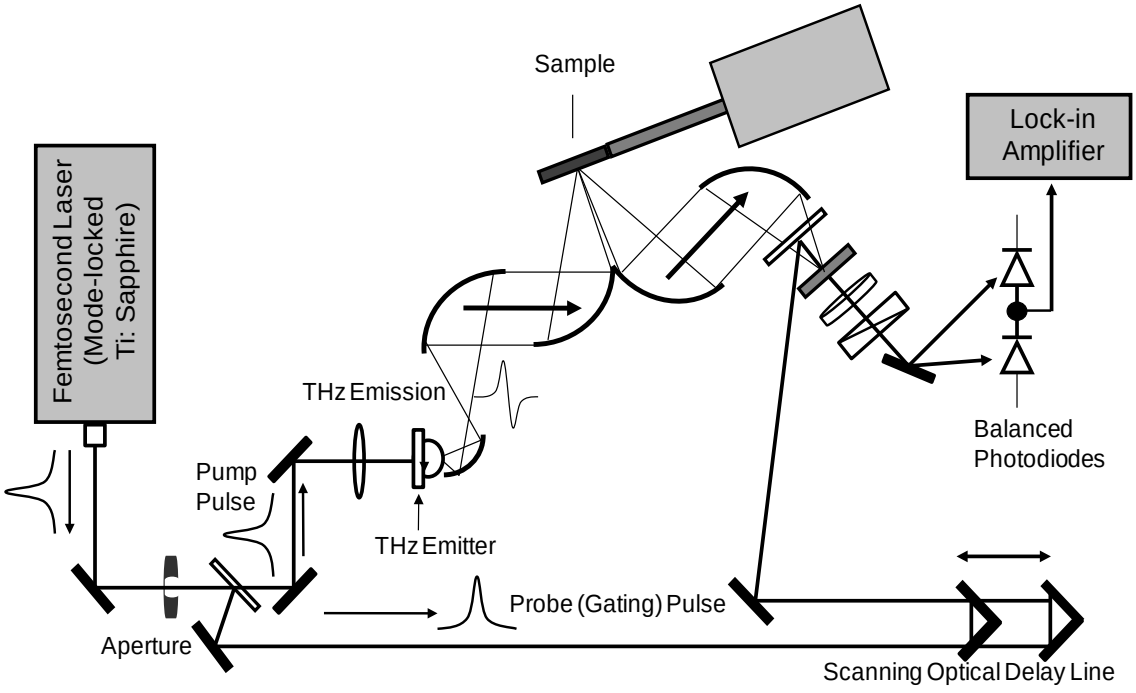

Figure 11. Reflective mode setup for pulsed THz imaging [7].

3.4.1.2 Lock-in Amplifier

The time domain pulses were measured as voltage data by the Stanford Research Systems Model SR850 DSP lock-in amplifier. A time constant of 30 ms and sampling rate of 64 Hz synchronized the data collection with the optical delay line providing a single pixel scan in 12 seconds. The lock-in amplifier then output the signal amplitude versus time to a computer where LabVIEW 8.2 data collection software saved each pixel scan as an individual data file.

3.4.2 THz Imaging Procedure

3.4.2.1 Sample Preparation

Once the test sample was vertically loaded into the Newmark NLS4 raster scanning system, it was aligned at a 20° angle to the incident radiation for maximum reflected beam collection. THz wavelengths are not visible so additional optics external to the THz system were used to direct a helium neon (HeNe) laser onto the focused THz beam spot location as a visual cue for vertical and horizontal sample alignment.

3.4.2.2 Biasing the Balanced Photodiodes

While blocking the path of the pump pulse prior to the PC switch, the pulsewidth of the beam was verified to be within the test range of 97-110 femtoseconds using a Pulse Check autocorrelator. The probe pulse was then used to adjust the voltage bias across the balanced photodiodes. Having connected the photodiode output to an oscilloscope and switched the photodiodes to the *Bal* setting, the input of the *signal* photodiode was blocked, and the voltage of the *reference* photodiode was set to -12 V as seen on the oscilloscope by slowly rotating the crystal attached to the back of the ZnTe detector (careful not to change the ZnTe crystal away from <110> alignment). Once achieved, the

signal photodiode was unblocked and the *reference* photodiode was then blocked. The voltage of the *signal* photodiode was then adjusted to +6 V by rotating the variable neutral density filter located directly in front of that photodiode (not pictured in Figures 10 and 11). The balanced photodiodes then displayed a reference bias of -6 V from the ground position and were switched back to the *AutoBal* setting. Finally, the balanced photodiode signal output was plugged back into the lock-in amplifier.

3.4.2.3 Optical Alignment

Before unblocking the pump pulse, its average power was verified to be below 45 mW to avoid damaging the PC switch THz emitter. Once accomplished, the optical delay was adjusted to the peak signal location by monitoring signal amplitude as displayed on the lock-in amplifier. Once found, the *AutoPhase* feature of the lock-in amplifier was used. Minor optical adjustments were then made as necessary to further maximize the peak signal strength.

IV. Results and Analysis

This chapter provides the results and analysis of the non-destructive evaluation of our fiberglass composite sample set for each of the five NDE methods. First, the results are presented and described. Then a detailed analysis of the images is performed arranged by damage type.

4.1 Radiography Results

The five shadowgraphs depicted in Figure 12 are the result of the frame averaging of 32 digital snapshots taken of each sample at a rate of 1 fps. Only one side of each sample was scanned. The lighter areas indicate higher material transmittance of X-rays while darker areas are regions of greater material absorption or scattering of X-rays. The image contrast provides information about the material's relative density and thickness. The digital images' contrast ratios were individually altered for better viewing of the internal structure and/or defects. No penetrant or dye was used to aid damage detection.

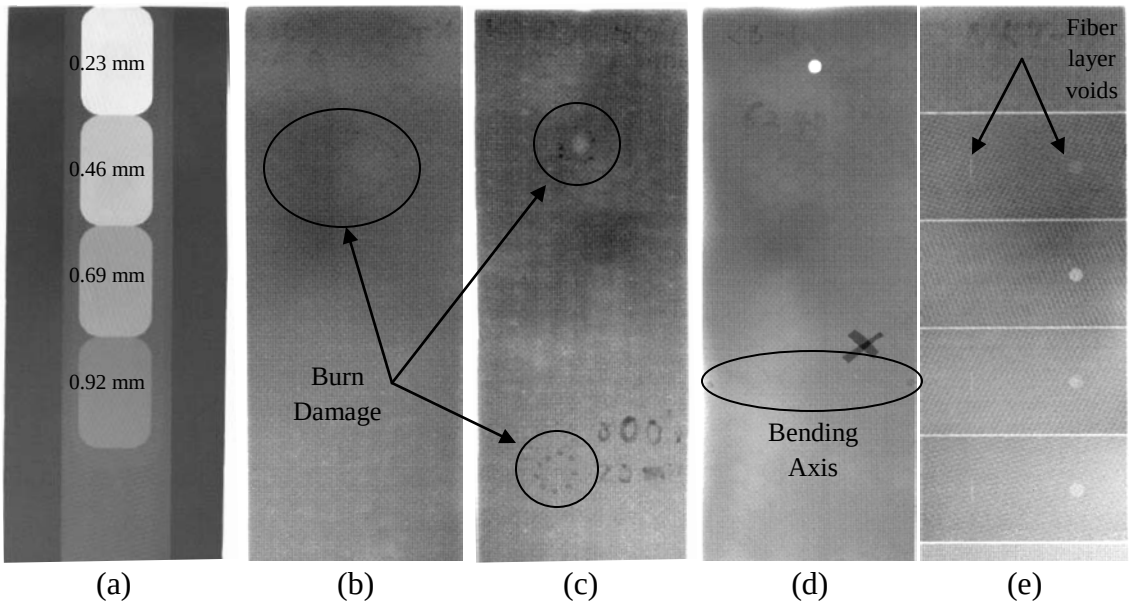

Figure 12. X-ray through scans of fiberglass composite samples showing front views of (a) thickness variation, (b) 4 minute 830°F burn damage, (c) 6 minute 810°F and 20 minute 800°F burn damage, (d) bending damage, and (e) sub-surface voids and delamination.

4.2 Radiography Analysis

4.2.1 Surface damage / thickness variation

X-ray inspection of the milled sample KT-4 (Figure 12a) clearly detected all six thickness regions. This shadowgraphic image can be used as a contrast standard for the images to follow. Each additional layer of composite material blocks more and more of the incident X-ray radiation so contrast differences in other samples can be compared to this thickness standard.

4.2.2 Heat damage

Three small regions of high heat concentration were analyzed—one near the top of sample KT-3, one near the top of sample KT-2, and one 2/3 the way down KT-2. Each burn on sample KT-2 is outlined with white paint dots.

There is a distinct line of contrast across each burn sample (Figures 12b and 12c) where the upper halves are darker than the lower. The line of contrast is due to the heat shielding used during sample preparation. Although sample KT-2 (Figure 12c) was burned on both halves, it still exhibits two distinct burn regions similar to KT-3 (Figure 12b). The reason lies in the thermal properties of the polyimide resin matrix. The burns were above the resin's glass transition temperature of ~750° F causing a density change in the matrix. The 800° F burn did not result in the same material density changes because the heat source was not kept in close enough contact to raise the matrix layers' temperatures above the glass transition temperature. The heat was dissipated laterally causing very small delaminations without affecting the density of the polyimide matrix.

The 4 minute, 830° F burn on sample KT-3 (Figure 12b) that produced surface bubbling and finish discoloration was barely detected after much effort in altering the digital image's contrast ratios. Only a dark oval, the burn spot boundary, is apparent. This delamination defect would not always be detected by radiography.

The 6 minute, 810° F burn spot near the top of sample KT-2 (Figure 12c) was detected as a 6 mm diameter light spot surrounded by black dots—the consequence of the white marker dots' high diffraction of X-ray photons.

The 20 minute, 800° F burn located near the bottom of sample KT-2 (Figure 12c) was not detected in multiple attempts with much effort to alter the contrast ratios. The only artifacts that appear are the marker dots and words "800° F 20 min" written in white paint on the sample. Also of note is the hexagonal pattern of glue remnants from when the samples were face sheets covering hexagonal-shaped tubes in a honeycomb matrix.

4.2.3 Mechanical damage

No damage was detected in sample KB-1 (Figure 12d) after two attempts, but the electrical tape *X* and the white marker dots at each end of the bend axis are quite visible. The 6,240 cycles of bending did not alter the density or thickness of the sample nor did they cause open cracks. X-rays were unable to detect the closed cracks (or micro-cracks) because the cracking didn't lead to a change in photon absorption or diffraction.

4.2.4 Sub-surface voids

All of the sub-surface voids on composite sample NKB-5 (Figure 12e) were detected on the second scan, the rectangular slits just visible. The contrast ratio was severely adjusted in order to show all of the defects simultaneously, the circular voids being much more apparent at normal contrast levels. In addition to the voids, transverse

dividing grooves were discovered evenly spaced between each set of milled regions. No other artifacts were captured, unlike with the other NDE methods.

4.2.5 Delamination

The open edge delamination at the top of sample NKB-5 (Figure 12e) was not detected. The delamination plane is parallel to the sample's front surface which was oriented perpendicular to the incident X-rays. Because the edge delamination did not lead to a change in density nor material thickness, it did not lead to a contrast difference from the surrounding material for detection. The sample was not rotated 90° to orient the X-rays along the plane of the delamination since the test sample was too thin for such a test with the equipment used. Such a test saturates the detector providing no useful structural information.

4.3 X-ray CT Results

The nine shadowgraphs depicted in Figure 13 are the result of 720 X-ray projections created by rotating the samples 360° in ½ angle increments within the X-ray beam. These are facial and cross-sectional snapshots of the three dimensional digital objects that are able to be rotated in 3D and *sliced* along a given plane. It was necessary to vary the digital images' contrast ratios to better view the internal structure and/or defects within the samples. The darker areas indicate higher transmittance of X-rays while lighter regions are areas of greater material absorption or diffraction of X-rays. The edge diffraction effects are artifacts of the X-ray method and allowed for easier detection of defects, but warping of the sample exaggerated the effect. No penetrant or dye was used to aid damage detection.

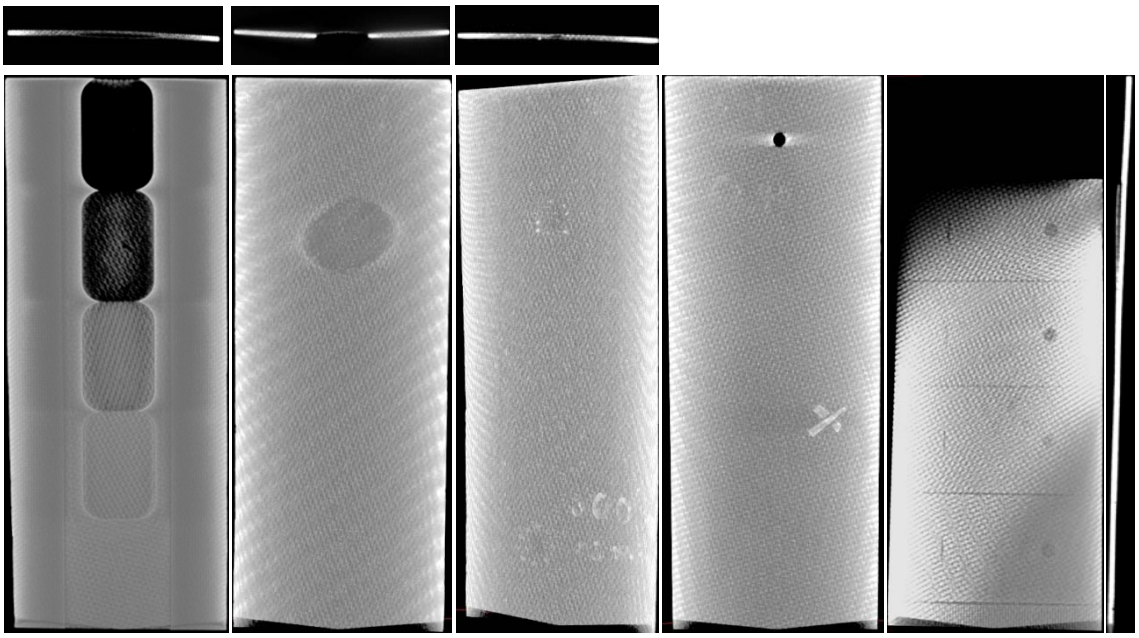

(a) (b) (c) (d) (e)

Figure 13. X-ray CT scans of fiberglass composite samples showing exterior and cross-sectional views of (a) thickness variation, (b) 4 minute 830°F burn damage, (c) 6 minute 810°F and 20 minute 800°F burn damage, (d) bending damage, and (e) sub-surface voids and delamination.

4.4 X-ray CT Analysis

4.4.1 Surface damage / thickness variation

Three dimensional X-ray inspection of the milled sample KT-4 (Figure 13a) clearly detected all six thickness regions. The edge diffraction effects appear blurred as the focus of the image is on the center milled section where the weave pattern of glass fiber bundles is readily apparent.

4.4.2 Heat damage

The 4 minute, 830° F burn on sample KT-3 (Figure 13b) is quite apparent in the CT scan. The area corresponding to the burn bubble is considerably darker than the surrounding material, while the burn boundary is outlined by lighter contrast edge diffraction further aiding defect detection. This defect was barely detected by radiography.

The 6 minute, 810° F burn near the top of sample KT-2 (Figure 13c) was detected as a small dark spot surrounded by white marker dots. The cross-sectional slice shows a small void was created beneath the burn.

The 20 minute, 800° F burn near the bottom of sample KT-2 was also detected. The marker dots and words “800 F 20 min” written in white paint on the sample were also captured. The cross-sectional views show very small air voids were created beneath the burn spot. The sharp line of contrast seen in the radiographic image was not captured by the X-ray CT scan.

4.4.3 Mechanical damage

Again, no damage in sample KB-1 (Figure 13d) was detected by the X-rays. The drilled hole at the top, the writing, and the electrical tape *X* are the only visible artifacts. Cross-sectional slice analysis did not reveal any additional information. It seems that the micro-cracking had little effect on the path of the X-rays causing neither increased scatter off material discontinuities nor decreased absorption through the crack’s lower density region. Longer test scans focused solely on the bend axis would provide greater resolution and might reveal evidence of physical damage.

4.4.4 Sub-surface voids

All of the sub-surface voids on NKB-5 (Figure 13e) were detected. Due to the warping of the sample, the image shown is a planar slice just inside the front surface—necessary to simultaneously view all of the defects. The transverse grooves are also viewable. Other artifacts captured are small, faint circles of greater material transmittance—the largest just below the sample’s center. These indicate local decreases in matrix density or possible disbonds between fiber and matrix layers.

4.4.5 Delamination

The edge delamination is apparent in the side, top, and cross-sectional slice views, but not from the front. The extent of the disbonding is difficult to measure or visualize from a single viewpoint. To fully investigate the extent of the damage, it is necessary to incrementally image cross-sectional slices until the defect is no longer detected.

4.5 Ultrasound Results

A 5 MHz, 3 inch focal length transducer scanned each sample in a pulse-echo ultrasound method using a reflector plate. The images shown in Figure 14 are the result of color-mapping the signal amplitude returning from the back reflector plate located behind the samples. Grey indicates the loss of signal while red indicates areas of maximum return signal amplitude. Samples (a), (b), and (c) have a front surface coating not present on samples (d) and (e). The surface coating exhibits much higher signal attenuation than the fiberglass weave and polyimide resin.

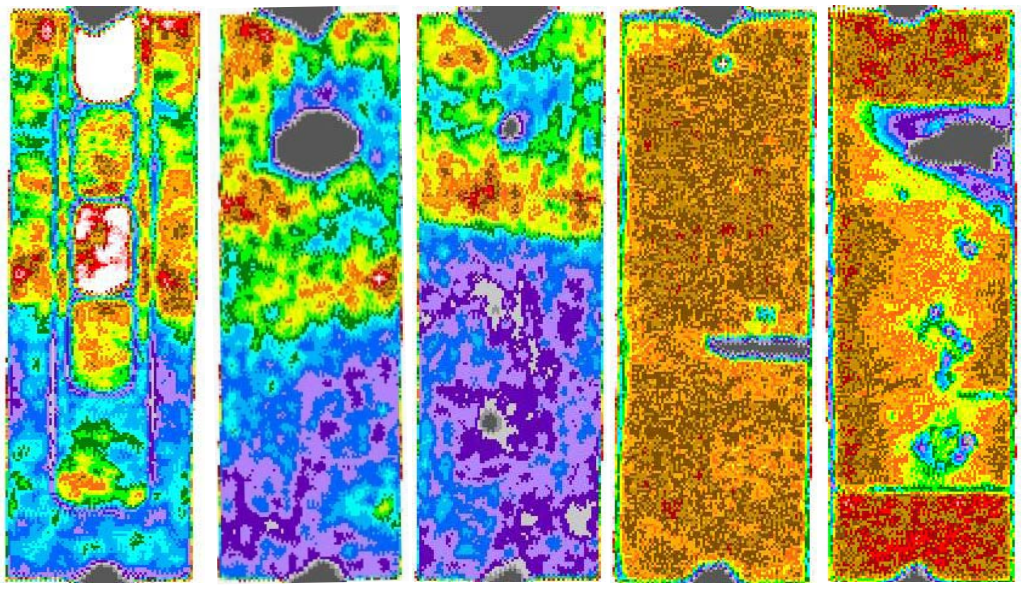

Figure 14. Ultrasonic scans of fiberglass composite samples at 5 MHz for (a) thickness variation, (b) 4 minute 830°F burn damage, (c) 6 minute 810°F and 20 minute 800°F burn damage, (d) bending damage, and (e) sub-surface voids and delamination.

4.6 Ultrasound Analysis

4.6.1 Surface damage / thickness variation

The milled sections of sample KT-4 (Figure 14a) are well-defined due to the low amplitude edge diffraction, but the varying thickness of the sample is not well depicted. The sections of 0.23 mm and 0.69 mm thickness provided equivalent return signal amplitudes, as did those of 0.46 mm and 0.92 mm making them appear to be of similar thickness.

4.6.2 Heat damage

The 4 minute, 830° F burn on sample KT-3 (Figure 14b) was easily detected. The return signal amplitude is zero for the burn damaged region, considerably different from the surrounding material.

The 6 minute, 810° F burn and 20 minute, 800° F burn on sample KT-2 (Figure 14c) were both detected as small, zero amplitude dark spots. The surrounding white marker dots were not resolved if detected at all.

4.6.3 Mechanical damage

The bending damage (Figure 14d) was clearly detected along half of the bend axis. The electrical tape *X* and drilled hole at the top were both detected as well—the hole as a maximum signal return surrounded by low returns and the tape as a low return region. It appears that only the center of the *X* where the tape strips overlapped was the return signal amplitude significantly altered.

The width of the damage region strongly suggests that the ultrasound did not detect the fiber breaks but the changes in matrix elastic properties. When reinforcement fibers break creating tiny disbonds, the surrounding matrix experiences localized yielding

as it is stressed beyond its elastic limit. Ultrasonic inspection is highly sensitive to material stiffness and elasticity. Matrix yielding would significantly slow and diminish the propagation of acoustic waves resulting in the local zero amplitude return signals at the detector within the time gate used.

4.6.4 Sub-surface voids

As seen in Figure 14e, three of the circular voids were detected while the fourth was masked by the open edge delamination signal return. The rectangular slits were not detected at all. The most surprising result was the detection of sub-surface porosity, and it was not located where it was expected—within the manufactured voids. Care was taken in manufacturing the sample to keep the bonding agent out of the milled voids by selectively applying less near the voids. Combined with a lack of appropriately applied pressure to this area during composite curing, this led to different matrix layer properties along the middle of the sample as is evident in the figure (lighter color in the middle than near edges, top, and bottom). Either there were air bubbles in the bonding agent or the air that was trapped in the milled voids between lamina layers displaced some of the bonding agent during the curing process. This left small air pockets or local delaminations in the layer between fiber lamina layers around the circular voids and showed up as dark spots in the ultrasound scan due to the extra scattering effects.

A likely explanation for the failure of the 5 MHz signal to detect the rectangular slits is that the acoustic wavelength in the material is approximately 1 mm (~5000 m/s acoustic velocity in the medium divided by the frequency of 5 MHz) which is twice the slit width, and as a general rule, $\lambda/2$ is the very minimum defect size ultrasound can detect [38].

4.6.5 Delamination

The delamination and extent of the disbonding is readily apparent (Figure 14e). The delamination extends beyond the first circular void, and its signal attenuation obscures the existence of the top circular void.

4.7 Flash IR Thermography Results

The grey-scale images of Figure 15 were individually selected from the 60 frame-per-second IR photography to best depict defect clarity. The results obtained are software enhanced and do not include direct surface temperatures; but instead, show the time rate-of-change of the front surface temperature as the temperature gradient is affected by sub-surface defects to a greater extent than the surface temperature itself.

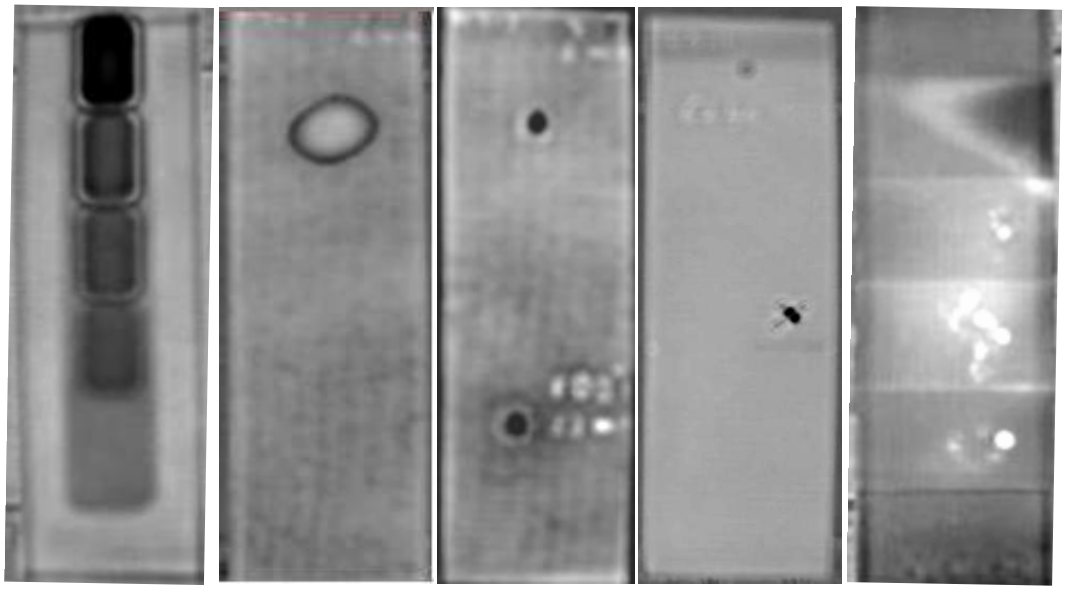

Figure 15. Flash IR thermographic images of time-derivative thermal conductivity for fiberglass composite samples showing: (a) thickness variation, (b) 4 minute 830°F burn damage, (c) 6 minute 810°F and 20 minute 800°F burn damage, (d) bending damage, and (e) sub-surface voids and delamination.

4.8 Flash IR Thermography Analysis

4.8.1 Surface damage / thickness variation

All six surface levels of sample KT-4 (Figure 15a) were distinguished simultaneously. This sample was then used as a thickness standard beside each of the other samples under inspection to capture artifact depth information.

4.8.2 Heat damage

All three burn defects on samples KT-2 and KT-3 (Figures 15b and c) were clearly detected. The time lapse imaging captured each defect's size, shape, and depth.

4.8.3 Mechanical damage

The damage was detected along only half the bend axis—that which has the electrical tape (Figure 15d). Though faint, the contrast was sufficient to recognize the defect as the heat dissipated from the surface. The time from initial heat flash until feature disappearance provided insight into the depth of cracking—surface cracking only.

4.8.4 Sub-surface voids

The results for sample NKB-5 (Figure 15e) look remarkably similar to those obtained under ultrasonic inspection. Three of the circular voids are clearly detected while the top fourth is obscured by the edge delamination. Only the two bottom rectangular slit voids, which are closest to the front surface, were detected. That result is consistent with decreased resolution of defects as the depth from front surface increases and lateral heat conduction becomes important. These line defects were very briefly visible and easily missed without previous knowledge of their locations. The circular artifacts have the same thermal properties as the voids, which further supports the idea that the artifacts are air voids or disbonds and not due to less dense bonding material.

4.8.5 Delamination

The delamination and extent of the disbonding was as readily apparent under the flash IR thermography (Figure 15e) as it was for the ultrasound method (Figure 14e). The delamination extended beyond the first circular void, and the signal attenuation obscured the existence of the top circular void.

4.9 THz Imaging Results

Figure 16 shows images of the reflected THz peak pulse amplitudes overlaid their respective positions on photographs of the composite samples. Figures 17-23 provide close-up views. The warm red and yellow colors correspond to high return signal values while the cool blue colors represent low return signal amplitudes. Unfortunately, time and technique limited the amount of surface area scanned. While the techniques used to produce these results are not realistic for large-scale NDE use, they do provide insight into the capabilities of the technology.

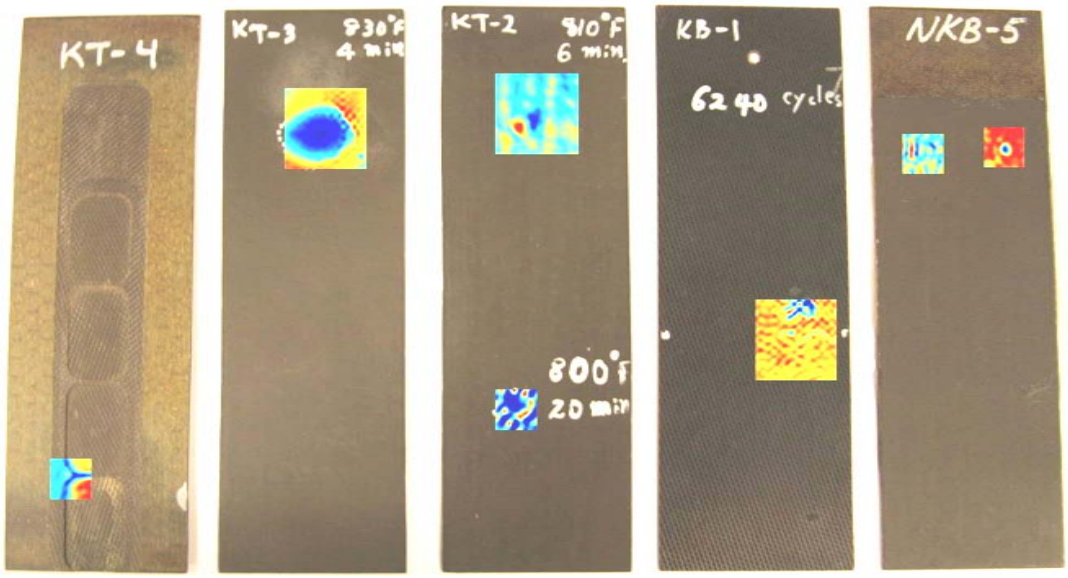

Figure 16. Pulsed THz imagery of fiberglass composite samples showing 1 cm^2 & 2 cm^2 scans of reflected peak pulse signal amplitudes overlaid on the respective test samples. Red colors correspond to peak return signal amplitude; blue corresponds to minimum return amplitude.

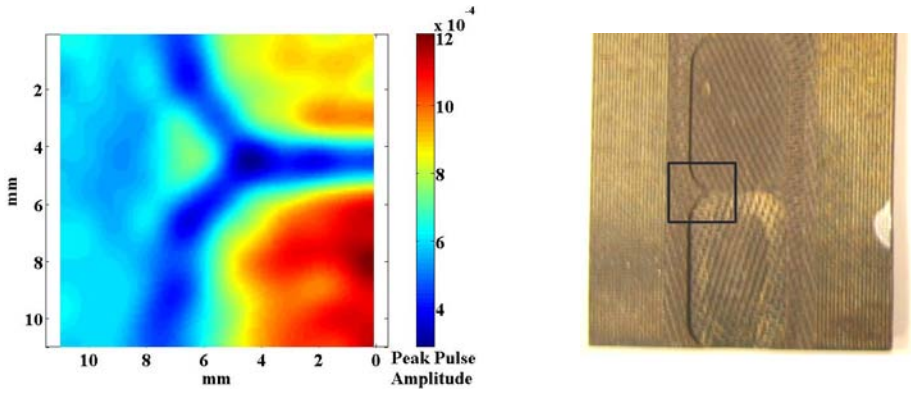

Figure 17. Pulsed THz imagery of a fiberglass sample showing reflected pulse amplitudes of thickness variations of 0.69 mm and 0.92 mm.

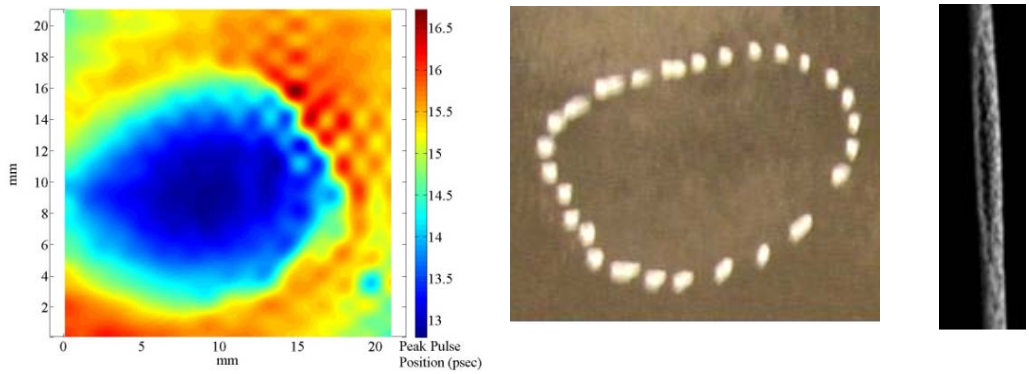

Figure 18. A fiberglass composite sample with a spot burned for 4 minutes at 830°F imaged with (a) pulsed THz imagery showing the return time delays of the reflected peak pulses, (b) still photography, and (c) X-ray Computed Tomography showing the internal cross-section.

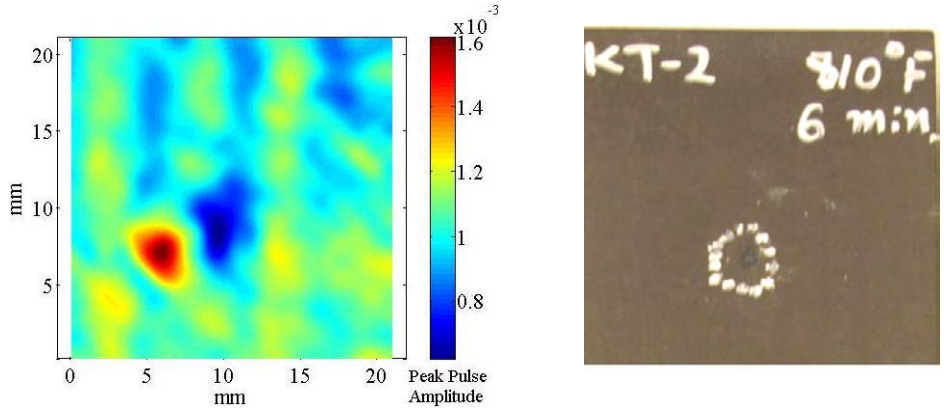

Figure 19. Pulsed THz imagery of a fiberglass sample showing reflected peak pulse amplitudes of 6 minute 810°F burn damage and white marker dots.

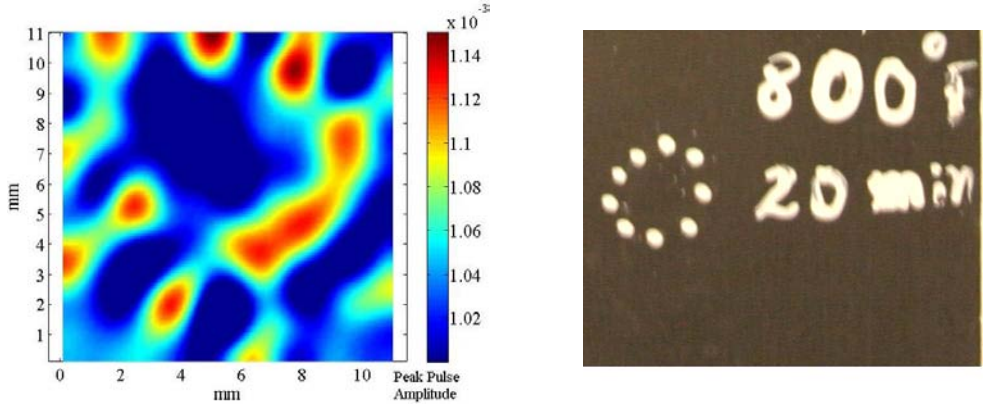

Figure 20. Pulsed THz imagery of a fiberglass sample showing reflected peak pulse amplitudes of 20 minute 800°F burn damage and white marker dots.

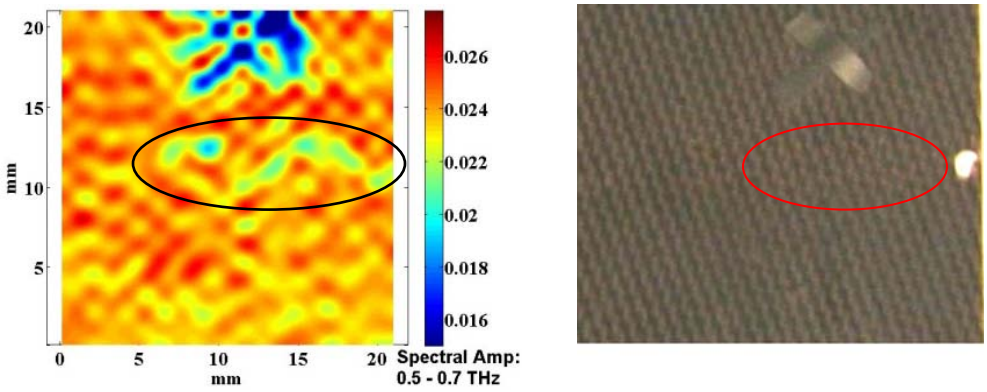

Figure 21. Pulsed THz imagery of a fiberglass composite sample showing a narrow frequency range of reflected pulse amplitudes of mechanical bending damage beneath electrical tape X.

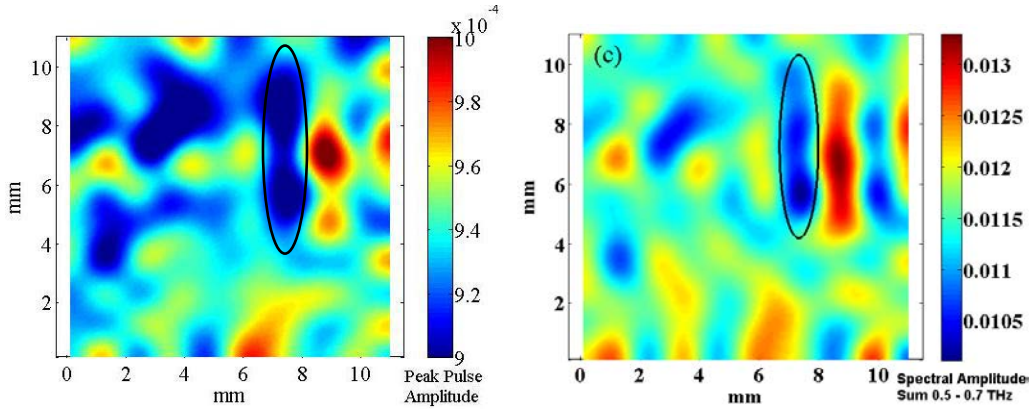

Figure 22. Pulsed THz imagery of a fiberglass sample showing reflected pulse amplitudes of a sub-surface rectangular void in (a) a broad THz frequency range and (b) a narrow THz frequency range.

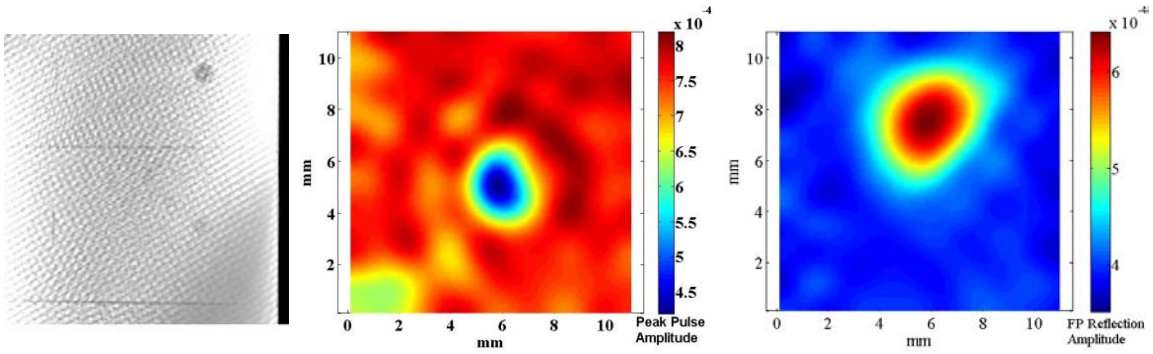

(a) (b) (c)

Figure 23. A fiberglass composite sample imaged with (a) X-ray CT depicting fiber structure and sub-surface defects while (b) and (c) are imaged by reflected THz radiation amplitudes from the area around a 3 mm diameter sub-surface circular void.

4.10 THz Imaging Analysis

4.10.1 Surface damage / thickness variation

Inspection of the milled sample KT-4 (Figure 17) clearly shows the ability of THz imaging to detect slight variations in object thickness. The edges of the milled regions are pronounced due to the size of THz beam spot used and the frequency dependence of edge diffraction. Narrowing the spot size and limiting the frequencies used would have sharpened the resolution near the edges.

4.10.2 Heat damage

The 4 minute, 830° F burn on sample KT-3 (Figure 18) was detected while providing excellent image contrast. It was best imaged in the time domain showing the time delay of the pulse's peak amplitude. This should have been expected since the burn caused the sample to blister creating a large air void leading to internal Fabry-Perot reflections of the radiation as discussed in section 2.5.2.

The image of the 6 minute, 810° F burn on sample KT-2 seen in Figure 19 shows the damage as a minimum signal value in the location corresponding to the burn residue. It is unclear why only one marker dot appears as an area of maximum signal return.

The 20 minute, 800° F burn spot (Figure 20) damage detection was inconclusive. While other NDE methods show small sub-surface delaminations within the ring of marker dots, the THz imaging of a 10 mm x 10 mm area had insufficient resolution to detect any differences in the material's structure. A larger area scan encompassing undamaged sample material would determine whether the entire area within the ring of marker dots was damaged or the THz system used is simply unable to detect this defect.

4.10.3 Mechanical damage

After several failed attempts to detect it, the bend damage (Figure 21) was eventually imaged as a jagged line of lower signal returns along the bend axis beneath the electrical tape *X* (accurately following visible surface cracks). No damage to the left of the tape was detected.

4.10.4 Sub-surface voids

The sub-surface circular void was detected as an Airy ring of decreasing return signal amplitudes at the center of the void location (Figure 23). An additional scan using the second pulse peak measuring Fabry-Perot reflections from the void was also successful in detecting the damage. The sub-surface slit void's detection is inconclusive in both scans (Figure 22) likely due to the 3.5 mm spot size of the THz beam.

4.10.5 Delamination

The edge delamination was not able to be imaged as it encompasses an area larger than the scan size limit of the THz system. Side profile scanning was not attempted as it would be dominated by diffraction and interference effects due to a beam spot size 3 times wider than sample thickness. Fabry-Perot reflection analysis was not attempted.

V. Comparisons and Conclusions

This chapter summarizes the research effort while providing a comparison guide of the NDE methods explored. It compares and contrasts the advantages and disadvantages of each technique in the evaluation of fiberglass composites. Finally, recommendations for additional research complete this thesis.

5.1 Comparisons

The results of THz imaging compared well to those of the conventional NDE techniques. A side-by-side image comparison of the test results is provided in Figure 24. A comparison guide to the five methods' damage detection effectiveness for fiberglass composites is provided by defect type in Table 1 followed by a discussion of the operational suitability of THz and ultrasonic imaging systems.

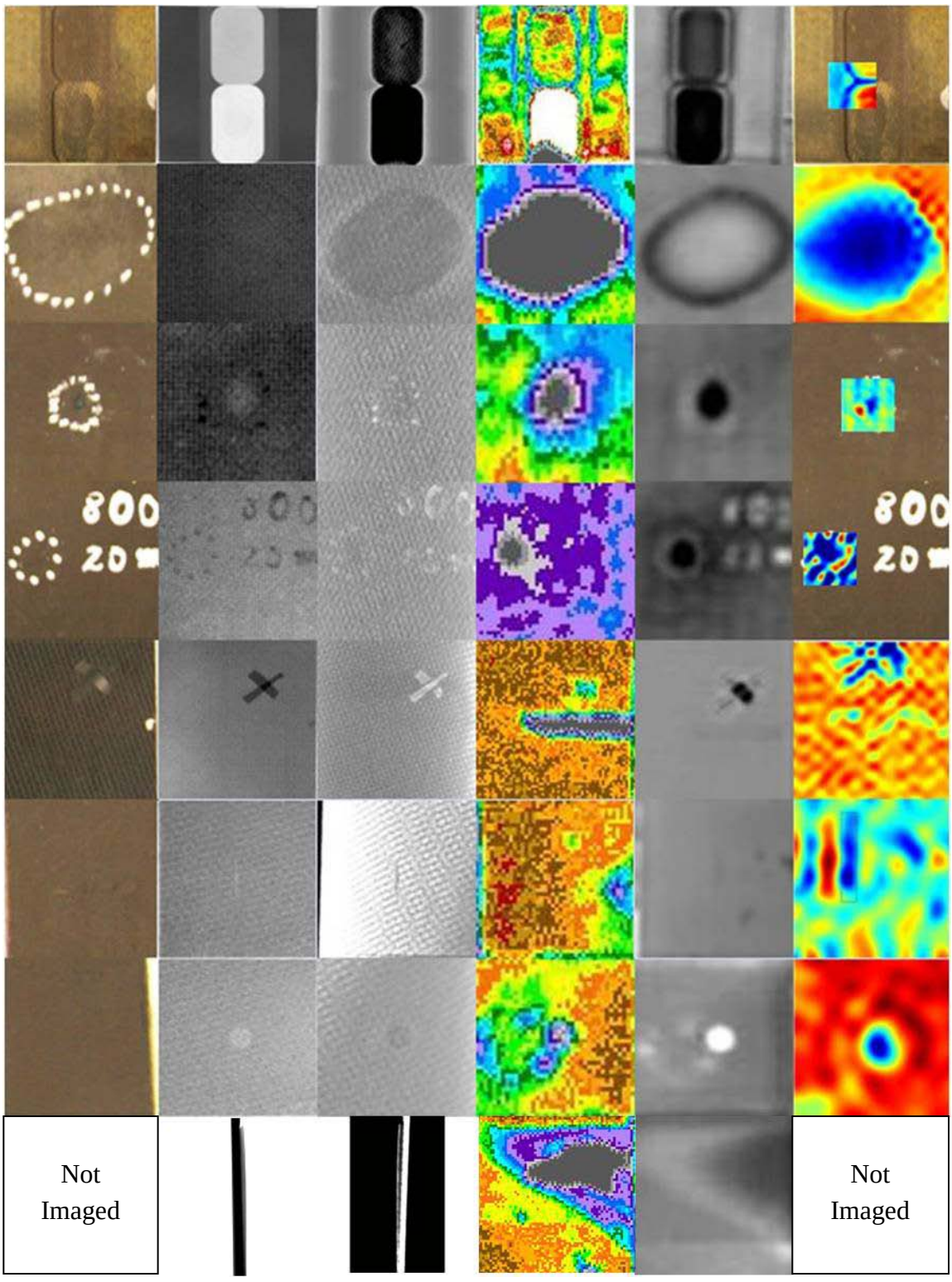

Figure 24. Image comparison chart of the damaged fiberglass composite sample set. From left to right, columns correspond to imaging with: photography, X-ray, X-ray CT, ultrasound, flash IR thermography, and THz imaging.

Table 1. Comparison of capabilities for the NDE of damaged fiberglass composite.

	X-ray	X-ray CT	Ultrasound (immersive pulse-echo)	Flash IR Thermography	Pulsed THz Imaging
Sensitivity to:					
Thickness Variation	Excellent	Excellent	Good	Excellent	Excellent
Burn Damage – Disbond / Air void	None	Excellent	Excellent	Excellent	Excellent
Burn Damage – Thermo-elastic yielding	Moderate	None	Excellent	None	*
Micro-cracking – Matrix yielding	None	None	Excellent	Moderate	Moderate
Sub-surface Voids	Good	Excellent	Moderate	Good	Good
Delaminations / Disbonds	Poor	Good	Excellent	Excellent	*

* Small scan area prevented analysis

The pulsed terahertz setup used, while a good demonstrator of THz imaging capability, was too sensitive to optical alignment and too limited in scan size and speed for operational use. This particular system was by no means the state of the art for THz imaging technology. Use of a TeraView TPI imaga 1000 or Picometrix T-Ray™ 4000 commercial THz materials characterization system (Figure 25) would have provided a full realization of the NDE capabilities of terahertz technology.

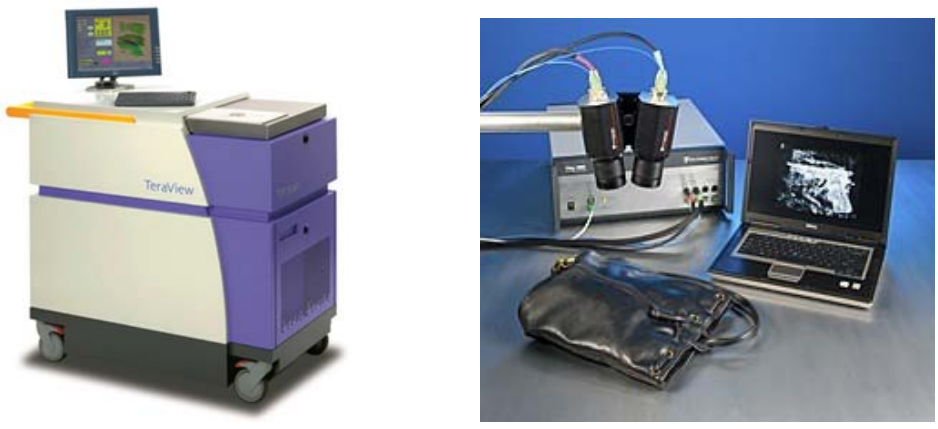

(a) (b)

Figure 25. Commercial systems for materials characterization: (a) TeraView TPI imaga 1000, (b) Picometrix T-Ray 4000 [34, 35].

Immersive pulse-echo ultrasound is not a production floor or flight hangar operation but is still an industrial standard technique. The cutting edge of acoustic NDE is in laser-ultrasonics, an emerging technology used by Lockheed Martin Corp. and the U.S. Air Force for inspection of thin polymer matrix composite parts in the F-22A Raptor. It provides higher resolution and adds curved surface inspection capability, but remains exceptionally complex and limited to near-surface evaluation. The advantages and disadvantages of all five NDE methods tested are summarized in Table 2.

Table 2. Comparison of advantages and disadvantages for various NDE methods.

	X-ray	**X-ray CT**	**Ultrasound (immersive pulse-echo)**	**Flash IR Thermography**	**Pulsed THz Imaging (Reflective mode demonstration setup)**
Advantages:	Non-Contact	Non-Contact	Inexpensive	Non-Contact	Non-Contact
	High Resolution	High resolution	Tuneable freq.	High resolution	High resolution
	Short scan time	3D volumetric images	Weak signal (Safe)	Simple setup & procedure	Weak radiation (Safe)
	Automated	Automated	Automated	Portable	Automated
	Inexpensive		Non-Ionizing	Non-Ionizing	Non-Ionizing
			Short scan time	Short scan time	Tuneable freq.
			Reflective scanning	Reflective scanning	Reflective scanning
				Inexpensive	Spectral analysis
Disadvantages:	Highly dangerous radiation	Highly dangerous radiation	Small scanning area	Short heat flash range	* Small scanning area
	High voltage danger	High voltage danger	Poor penetration depth	Poor penetration depth	* Complex optical setup
	Ionization of target and surrounding area	Ionization of target and surrounding area	Sensitivity to alignment – no curved geometries	High sensitivity to surface geometry	High sensitivity to surface geometry
	Requires access to opposing surfaces	Requires 360° access	Coupling gel or liquid required	Ineffective for wet or metal materials	Ineffective for wet or metal materials
		Expensive	Low Resolution	Ineffective for variable emissivity	Expensive

* Not applicable to alternate or commercial THz systems

5.2 Conclusions

Five methods of non-destructive evaluation were used to inspect various forms of damage to aerospace fiberglass composite samples. The conventional NDE methods of X-ray, X-ray CT, ultrasound, and flash IR thermography were compared to the emerging technology of THz imaging to evaluate its utility in composite material inspection. The resulting images were analyzed and compared while each method's respective advantages, disadvantages, capabilities, and limitations were explored.

Although the comparisons made in this thesis are by no means a complete picture of these NDE methods' full capabilities in composite evaluation, we have made great distinctions in their abilities to detect common damage mechanisms in fiberglass. Ultrasonic inspection was the best overall evaluation method. Next best in effectiveness was flash IR thermography followed by THz imaging, X-ray CT, and X-ray. For inspections of thin fiberglass composites in an operational environment, only flash IR thermography or a commercial THz imaging system would be practical for high resolution damage detection and imaging.

Pulsed THz imaging, when coupled with its time domain spectroscopy (TDS) ability, is able to provide more NDE capability than any other single technology. It effectively provides three simultaneous damage detection schemes in a single scan via return signal amplitude, phase, and frequency. It is capable of detecting all of the common aerospace composite defects: surface damage, delaminations, air voids, cracking, and burn damage. THz imaging even outperforms X-ray inspection. This technology definitely has an exciting future in the non-destructive evaluation of aerospace composite materials.

5.3 Recommendations for future work

Future work should expand the dataset as well as include continuous wave (CW) THz imaging as a sixth NDE method. The work should also investigate other common aerospace materials such as carbon and aramid fiber reinforced polymer composites. The results of such an effort would be improved by an enhanced THz imaging system. Particularly, the pulsed THz system should have an expanded scanning area for full sample scans, decreased scan times, and a smaller THz beam spot size. Greater THz signal amplitudes would improve signal-to-noise ratios and allow deeper evaluation of these denser composites as they are less transparent to terahertz frequency light.

Bibliography

1. Campbell, M. and Heilweil, E. Non-invasive detection of weapons of mass destruction using THz radiation. *SPIE.* 2003, Vol. 5070.

2. Watanabe, Yuuki and al., et. Spatial pattern separation of chemicals and frequency-independent components by terahertz spectroscopic imaging. *Applied Optics.* 2003, Vol. 42, 28.

3. Nishizawa, J. and et. al. THz imaging of nucleobases and cancerous tissue using a GaP THz-wave generator. *Optics Communications.* 2005, Vol. 244, 6, pp. 469-474.

4. Yan, Z. and al., et. Research progress of terahertz wave technology in food inspection. *SPIE.* 2006, Vol. 6373, p. 63730R.

5. Anastasi, R. Investigation of fiber waviness in a thick glass composite beam using THz NDE. *SPIE.* 2008, Vol. 6934, p. 69340K.

6. The Boeing Company. *Boeing 787 Dreamliner Program Fact Sheet.* [Online] [Cited: Feb 5, 2009.] http://www.boeing.com/commercial/787family/programfacts.html.

7. Stoik, C. *PhD Nondestructive Evaluation of Aircraft Composites Using Terahertz Time Domain Spectroscopy.*Air Force Institute of Technology, Wright-Patterson AFB OH, December 2008.

8. Mallick, P. *Fiber-reinforced composites: Materials, Manufacturing, and Design.* 3rd Ed. New York: CRC Press, 2008.

9. National Research Council. *Aging of U.S. Air Force Aircraft: Final Report.* Washington D.C.: National Academies Press, 1997.

10. Masters, J. *Damage detection in composite materials.* West Conchohocken, PA: ASTM International, 1993.

11. Hu, B. and Nuss, M. Imaging with terahertz waves. *Optics Letters.* 1995, Vol. 20, 16, pp. 1716-18.

12. Summerscales, J. NDT of advanced composites - an overview of the possibilities. *British Journal of NDT.* 1990, Vol. 32, 11, pp. 568-577.

13. Fletcher, J., Swift, G. and Chamberlain, J. Propagation of terahertz radiation through random structures: an alternative theoretical approach and experimental validation. *Journal of Applied Physics.* 2007, 101, 013102.

14. Pearce, J. and Mittleman, D. Scale model experimentation: using terahertz pulses to study light scattering. *Physics in Medicine and Biology.* 2002, 47, pp. 3823-30.

15. Bogan, S. and Hinders, M. *Interface Effects in Elastic Wave Scattering.* Berlin: Springer-Verlag, 1994.

16. Kerker, M. *The Scattering of Light and other Electromagnetic Radiation.* London: Academic Press, 1969.

17. Hanke, R., Fuchs, T. and Uhlmann, N. X-ray based methods for non-destructive testing and material characterization. *Nuclear Instruments and Methods in Physics Research A.* 2008, 591, pp. 14-18.

18. Miracle, D. *ASM Handbook Vol. 21: Composites.* New York: ASM International, 2001.

19. Backis, C. *Composite Materials: Testing and Design, Vol 14.* West Conshohocken, PA: ASTM International, 2003. pp. 29-34.

20. Ciliberto, A., et. al. Porosity detection in composite aeronautical structures. *Infrared Physics & Technology.* 2002, 43, pp. 139-143.

21. Ferguson, B. T-ray computed tomography. *Optics Letters.* 2002, Vol. 27, 15, pp. 1312-14.

22. Chau, K., Mujumdar, S. and Elezzabi, A. Terahertz propagation in non-homogeneous strongly scattering media. *SPIE.* 2005, Vol. 5727, pp. 177-183.

23. Woodward, R., Wallace, V. and et. al. Terahertz pulsed imaging of skin cancer in the time and frequency domain. *Journal of Biological Physics.* 2003, Vol. 29, 2/3, pp. 257-262.

24. *Terahertz Science & Technology Network web page.* [Online] [Cited: Feb 7, 2009.] http://www.thznetwork.org/wordpress/index.php/archives/304.

25. Medical Imaging. *TeraView web page.* [Online] [Cited: Feb 7, 2009.] http://www.teraview.com/terahertz/id/34.

26. Karpowicz, N., Zhong, H., et. al. Comparison between pulsed terahertz time-domain imaging and continuous wave terahertz imaging. *Semiconductor Science and Technology.* 2005, 20, pp. S203-S299.

27. Mittleman, D., et al. T-ray tomography. *Optics Letters.* 1997, Vol. 22, 12, pp. 679-92.

28. THz Optoelectronics: Imaging. *Rensselaer Center for Terahertz Research web page.* [Online] [Cited: Feb 5, 2009.] http://www.rpi.edu/terahertz/res_imaging.html.

29. Shen, Y., et. al. Generation and detection of ultrbroadband terahertz radiation using photoconductive emitters and receivers. *Applied Physics Letters.* 2004, Vol. 85, 2.

30. Mittleman, D., Jacobsen, R. and Nuss, M. T-ray imaging. *IEEE Journal of Selected Topics in Quantum Electronics.* 1996, Vol. 2, 3, pp. 679-692.

31. Mueller, E. Terahertz radiation: applicationa and sources. *The Industrial Physicist.* 2003, August/September, pp. 27-29.

32. Xin, X., et. al. Terahertz absorption spectrum of para and ortho water vapors at different humidities at room temperature. *Journal of Applied Physics.* 2006, 100, 094905.

33. Wu, D. and Meyer, J. Terahertz emission, detection and military applications. *SPIE.* 2004, Vol. 5411, pp. 187-195.

34. TPI imaga 1000 Product Sheet. *TeraView web page.* [Online] [Cited: Feb 6, 2009.] http://www.teraview.com/terahertz/id/21.

35. T-Ray 4000 Product Sheet. *Picometrix web page.* [Online] [Cited: Feb 8, 2009.] http://picometrix.com/pico_products/terahertz_tr4000.asp.

36. Amaro, A., Santos, J. and Cirne, J. Comparative study of different non-destructive testing techniques in the characterization and quantification of the damage effects in carbon-epoxy laminates. *Insight.* 2004, Vol. 46, 9, pp. 559-565.

37. Blitz, J. and Simpson, G. *Ultrasonic Methods of Non-destructive Testing.* New York: Chapman & Hall, 1996.

38. Collaboration for NDT Education. *Wavelength and Defect Detection*. [Online] [Cited: Feb 24, 2009] http://www.ndt-ed.org/EducationResources/CommunityCollege/Ultrasonics/Physics/defectdetect.htm.

Vita

Captain Jeremy D. Johnson graduated from Blue Ridge High School in Farmer City, Illinois in 1998. He attended Illinois College for three years earning a Bachelor of Science degree in Physics & Engineering before transferring to the University of Illinois at Urbana-Champaign to study structural mechanics. He graduated from the U of I in 2003 with a Bachelor of Science degree in Engineering Mechanics. Within months of graduation, he entered the U.S. Air Force Officer Training School (OTS) earning Honor Flight recognition and was commissioned a second lieutenant in the U.S. Air Force.

His first assignment was at Eglin AFB, Florida as a flight test engineer in the 40th Flight Test Squadron. He planned and executed the developmental flight testing of advanced munitions, sensors, and software aboard the F-15E Strike Eagle and UH-1N Huey helicopter and accumulated sufficient flight hours to earn non-rated aircrew wings. In 2007, he moved to Wright-Patterson AFB, Ohio to attend the Air Force Institute of Technology (AFIT) and earn a Master of Science in Materials Science. Upon completion of his MS degree, Capt Johnson will be assigned to the Sensors Directorate of the Air Force Research Labs (AFRL) at Wright-Patterson AFB, Ohio.

REPORT DOCUMENTATION PAGE

Form Approved
OMB No. 074-0188

1. REPORT DATE *(DD-MM-YYYY)*	**2. REPORT TYPE**	**3. DATES COVERED** *(From – To)*
26-03-2009	Master's Thesis	May 2007 – Mar 2009

4. TITLE AND SUBTITLE
Non-Destructive Evaluation of Aerospace Composites

5a. CONTRACT NUMBER

5b. GRANT NUMBER

5c. PROGRAM ELEMENT NUMBER

6. AUTHOR(S)
Johnson, Jeremy D., Capt, USAF

5d. PROJECT NUMBER

5e. TASK NUMBER

5f. WORK UNIT NUMBER

7. PERFORMING ORGANIZATION NAMES(S) AND ADDRESS(S)
Air Force Institute of Technology
Graduate School of Engineering and Management (AFIT/EN)
2950 Hobson Way
WPAFB, OH 45433-7765

8. PERFORMING ORGANIZATION REPORT NUMBER
AFIT/GMS/ENP/09-M02

9. SPONSORING/MONITORING AGENCY NAME(S) AND ADDRESS(ES)
James L. Blackshire, Ph.D. NDE Branch
Air Force Research Laboratory
Materials and Manufacturing Directorate
WPAFB, OH 45433-7750

Gernot Pomrenke, Ph.D. Physics & Electronics Directorate
Air Force Office of Scientific Research
875 N. Randolph St.
Arlington, VA 22203-1768

10. SPONSOR/MONITOR'S ACRONYM(S)
AFRL/RXLP AFOSR/NE

11. SPONSOR/MONITOR'S REPORT NUMBER(S)

12. DISTRIBUTION/AVAILABILITY STATEMENT

APPROVED FOR PUBLIC RELEASE; DISTRIBUTION UNLIMITED

13. SUPPLEMENTARY NOTES
This material is declared a work of the U.S. Government and is not subject to copyright protection in the United States.

14. ABSTRACT

Five methods of non-destructive material evaluation (NDE) were used to inspect various forms of damage commonly found in aerospace fiberglass composites: voids, edge and sub-surface delaminations, surface burning, and cracking. The images produced by X-ray, X-ray Computed Tomography, terahertz (THz) imaging, ultrasound, and flash IR thermography were analyzed for the detection of defects. Test results and analysis of each NDE method's capabilities provide a comparison study of conventional techniques versus the emerging technology of THz imaging for the non-destructive evaluation of aerospace composite materials. A comparison guide to the five methods' damage detection effectiveness for fiberglass composites is provided by defect type.

15. SUBJECT TERMS
Non-destructive evaluation (NDE), terahertz (THz), THz imaging, X-ray, X-ray Computed Tomography (X-ray CT), flash IR thermography, ultrasound, composite materials, defect detection, material defect imaging

16. SECURITY CLASSIFICATION OF:			**17. LIMITATION OF ABSTRACT**	**18. NUMBER OF PAGES**	**19a. NAME OF RESPONSIBLE PERSON**
REPORT	**ABSTRACT**	**c. THIS PAGE**			Matthew J. Bohn, Lt Col, USAF (ENP)
U	**U**	**U**	**UU**	72	**19b. TELEPHONE NUMBER** *(Include area code)* (937) 255-3636 x4573 matthew.bohn@afit.edu

Standard Form 298 (Rev: 8-98)
Prescribed by ANSI Std. Z39-18